Front. Energy 2022, 16(4): 548–580
https://doi.org/10.1007/s11708-022-0826-8

REVIEW ARTICLE

Muni Raj MAURYA, John-John CABIBIHAN, Kishor Kumar SADASIVUNI, Kalim DESHMUKH

A review on high performance photovoltaic cells and strategies for improving their efficiency

Abstract The introduction of a practical solar cell by Bell Laboratory, which had an efficiency of approximately 6%, signified photovoltaic technology as a potentially viable energy source. Continuous efforts have been made to increase power conversion efficiency (PCE). In the present review, the advances made in solar cells (SCs) are summarized. Material and device engineering are described for achieving enhanced light absorption, electrical properties, stability and higher PCE in SCs. The strategies in materials and coating techniques for large area deposition are further elaborated, which is expected to be helpful for realizing high-efficiency SCs. The methods of light-harvesting in SCs via anti-reflecting coatings, surface texturing, patterned growth of nanostructure, and plasmonics are discussed. Moreover, progress in mechanical methods that are used for sun tracking are elaborated. The assistance of the above two protocols in maximizing the power output of SCs are discussed in detail. Finally, further research efforts needed to overcome roadblocks in commercialization were highlighted and perspectives on the future development of this rapidly advancing field are offered.

Keywords photovoltaic, efficiency, large area deposition, light harvesting, sun tracker

Received Jul. 15, 2021; accepted Dec. 31, 2021; online May 20, 2022

Muni Raj MAURYA
Mechanical and Industrial Engineering Department, College of Engineering, Qatar University, Doha 2713, Qatar; Center for Advanced Materials Qatar University, Doha 2713, Qatar

John-John CABIBIHAN (✉)
Mechanical and Industrial Engineering Department, College of Engineering, Qatar University, Doha 2713, Qatar
E-mail: john.cabibihan@qu.edu.qa

Kishor Kumar SADASIVUNI (✉)
Center for Advanced Materials, Qatar University, Doha 2713, Qatar
E-mail: kishor_kumars@yahoo.com

Kalim DESHMUKH
New Technologies-Research Center, University of West Bohemia, Plzen 30100, Czech Republic

1 Introduction

The consumption of non-renewable energy is rapidly increasing. According to the statistical review of World Energy 2020, fossil fuels accounted for 84% of the world's primary energy consumption in 2019 [1]. Consequently, this contributes to the problem of global warming. There are limited non-renewable sources available; its eminent depletion has made the international community focus on other sustainable energy sources. Thus, the research community has been continuously working to produce energy from renewable resources like sun, water, wind, etc. among which, the abundant presence of solar energy worldwide makes it a promising candidate to fulfill the energy needs of future generations without any adverse effect on the environment. Under this context, the conversion of sunlight into electricity, often called photovoltaic (PV) or the solar cell (SC) technology offers an environment-friendly way to convert photon energy into electricity directly [2]. In 1839, French physicist Edmund Bequerel observed the photoelectric effect and reported certain materials which could generate small amounts of electric current under light exposure [3]. Based on this concept, in 1954, Bell Laboratories fabricated the first practical SC using diffused silicon (Si) p-n junctions, with an efficiency of 6%. The power convergence efficiency (PCE) measures the efficiency of SC in converting solar spectrum and is given by Eq. (1) [4].

$$\mathrm{PCE} = \frac{J_{\mathrm{sc}} \times V_{\mathrm{oc}} \times \mathrm{FF}}{P_{\mathrm{in}}} \times 100\%, \tag{1}$$

where FF represents the fill factor, V_{oc} is defined as the open-circuit voltage, J_{sc} is the current density under no load, and P_{in} is the incident light power. The efficiency of SC can be improved by simultaneous enhancement of the J_{sc}, V_{oc}, and FF. This can be achieved by incorporating suitable band-gap materials covering the maximum range of the solar spectrum, deposition of high-quality photoactive (PA) material film, interfacial engineering,

thereby reducing the defect states. The current density is proportional to the number of photogenerated charge carriers, which strongly depends on the photon absorption ability and absorption range of the PA material. The basic SC is the single p-n junction device, and there is a limit for light to electrical conversion, which is determined by the Shockley-Queisser (SQ) model [5]. The maximum theoretical efficiency of Si SC estimated by the SQ model is approximately 30% [5]. The SQ model based PCE calculation takes solar spectrum, optical absorption, and SC operating temperature as inputs and considers their ideal values. Thus, as the properties of the real PA material vary from the ideal case, the practical single p-n junction-based SC will always have PCE below the SQ limit. As a result, the current density will always be lower than that of the ideal case. For single p-n junction SCs, the output current density with a resistive load is given by Eq. (2) [6].

$$J = J_{\mathrm{L}} - J_{\mathrm{o}}\left[\left(\mathrm{e}^{\frac{q(V+JR_{\mathrm{s}})}{AkT}}\right) - 1\right] - \frac{V + JR_{\mathrm{s}}}{R_{\mathrm{SH}}}, \tag{2}$$

$$J_{\mathrm{d}} = J_{\mathrm{o}}\left[\left(\mathrm{e}^{\frac{q(V+JR_{\mathrm{s}})}{AkT}}\right) - 1\right], \tag{3}$$

where J_{o} is the reverse saturation current density, J_{L} is the photovoltaic current density, J is the load current density, J_{d} is the junction current density of diode, R_{SH} is the parallel resistance, R_{s} is the series resistance, A is the factor of diode quality, T is the absolute temperature, k is the Boltzmann constant, and q is the electronic charge. The series resistance accounts for the bulk resistance of the PA material and the contact resistance of the metal electrode with the PA film. The shunt resistance is caused by the non-ideal p-n junction and impurities near the junction, which leads to partial shorting. Another important parameter factor that directly affects the PCE of SC is V_{oc}, given by Eq. (4) [7].

$$V_{\mathrm{oc}} = \frac{kT}{q}\ln\left(\frac{J_{\mathrm{L}}}{J_{\mathrm{o}}} + 1\right) \approx \frac{kT}{q}\ln\left(\frac{J_{\mathrm{L}}}{J_{\mathrm{o}}}\right), \tag{4}$$

where V_{oc} in the SCs is primarily controlled by the reverse saturation current density, J_{o}. J_{o} is the diode saturation current density under reverse bias, often called leakage current, and corresponds to the recombination of minority carriers across the junction. The leakage current has a $q/(kT)$ factor. Thus, it can be inferred that open V_{oc} decreases with an increase in the temperature. As a result, SCs have a negative temperature coefficient for V_{oc}. FF signifies the efficiency of the photogenerated charge carriers in reaching their respective electrodes, which is estimated from the current-voltage (I-V) curve [8]. Overall, the key processes affecting J_{sc}, V_{oc}, and FF, which in turn governs the efficiency of the SCs can be summarized as ① the solar spectrum absorptivity of PA material and its ability to generate electron-hole pairs [9–13], ② the effective separation and transportation of photogenerated charge [14–18], ③ the interfacial engineering for collection of charge carrier at respective electrodes [19–22], and ④ the control of the SC operating temperature [23–25]. Nowadays, researchers are developing large scale fabrication of SC with low cost and high efficiency. In this regard, they have studied various combinations of chemical and physical engineering to improve the PCE of the SC. In the present review, the various modifications adopted to enhance the efficiency of SCs have been discussed. The various topics covered under this include different types of PA materials and nanostructures layers incorporated to improve the spectral responsivity of the device and efficient collection of generated charge carriers, respectively. It also covers methods to improve the light-harvesting in SC and efficient technological advancement for large-area fabrication of SCs. Overall, the review gives a broader picture of the existing state-of-the-art technologies for the fabrication of highly efficient SC.

2 Progress in solar power convergence efficiency

The SC efficiency mainly depends on the efficient broad range absorption of the solar spectrum radiation reaching the earth's surface, thereby generating the photogenerated charge carriers and their collection at the respective electrodes. To achieve this, the PA material must be of high quality with the direct bandgap ranging between 1.1 and 1.7 eV and highly stable [26]. Various PA materials have been explored, and based on the type and nature of materials, the SCs are classified into three different generations (Fig. 1). The first-generation SCs are based on the simple p-n junction contact configuration, where mono or polycrystalline bulk Si is used as a PA material. The second-generation SC is based on the thin-film technology, which includes families of materials like amorphous/microcrystalline Si (a/μc-Si) SCs, copper indium gallium selenide (CIGS)/copper indium selenide (CIS), and cadmium telluride (CdTe)/cadmium sulfate (CdS), among others. The third generation are cost-effective SCs designed for high-efficiency extraction. The various photovoltaic cells in this generation are classified as organic or polymer SCs (OSCs), dye-sensitized SCs (DSSCs), perovskite SCs (PSCs), and multi-junction SCs, among others.

2.1 First generation SC

The first generation SCs used mono/poly crystalline Si and gallium arsenide (GaAs) as the PA material for device fabrication. In comparison to the 1.43 eV direct band-gap of GaAs, Si has a bandgap of 1.1 eV and the absorption of light is weaker in the latter case [26]. Despite this, the solar technology was initiated with Si

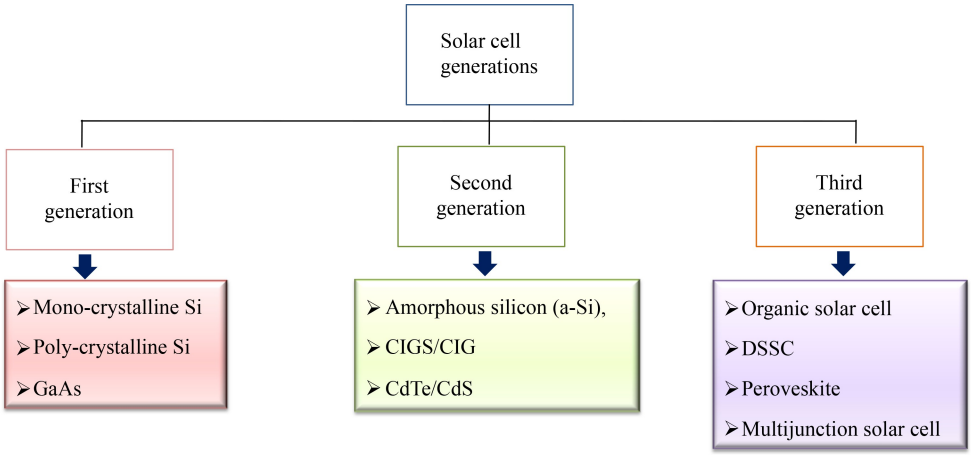

Fig. 1 Photo-absorbing materials-based classification of SC technologies in various generations.

and still holds a majority of the market. This is because there is a physical limitation of using the highly crystalline and high purity material for enhancing the efficiency of SC. During the initial stages of the photovoltaic cell, the Si technology was already established in terms of producing high-quality materials on a large scale. Moreover, Si is an abundant material, non-toxic, quite stable, and Si SCs would be compatible with the well-established Si-based microelectronics industry [27,28]. As a result, the research was confined to the Si-based SC and ways to improve their efficiency until new materials were investigated.

2.1.1 Mono-crystalline silicon solar cells

The highly pure Si ingot is produced from the small mono-crystalline Si (m-Si) seeds by the Czochralski process and later cut into wafers [26]. The first m-Si SC was reported in 1954 with an efficiency of 6%. With decades of research efforts, the m-Si SC with an efficiency greater than 25% was reported [29]. Recently, a large-area Si SCs combining interdigitated back contacts and an amorphous/crystalline Si heterojunction were fabricated with an efficiency of 26.3% (see Fig. 2) [29]. These SCs have a high conversion efficiency as they use high purity m-Si called solar grade silicon. The technology is very reliable; however, their manufacturing cost is high, requiring more energy during their life cycle due to heat losses via radiation/conduction [30–35].

2.1.2 Poly-crystalline silicon solar cells

Several other cost-effective methods were adopted to produce crystalline Si (c-Si), which will eventually reduce the fabrication cost of the m-Si based SCs. During this time, the concept of using poly-crystalline Si (p-Si) as the PA material came into existence and became more attractive. The p-Si based SC has an efficiency of ~20.4% and is somewhat less efficient than m-Si [36]. This is due to the presence of randomly oriented small Si crystals with smaller grain boundaries, defects, and high concentration of impurities. As a result, charge recombination centers are increased, which in turn decreases the current and lowers the voltage. With the introduction of p-Si, the cost of manufacturing was reduced in comparison to the m-Si. The other merits include a lesser greenhouse effect and less energy requirement in its production [30–35]. The SC technology history was reviewed by Goetzberger and Hebling [26], and the future prospects of the technology were covered using Si as a PA material. The advances in the metallurgical and chemical methods for the production of Si were reviewed by Braga et al. [37] who emphasized that the solar grade Si is more efficient for the fabrication of high-efficiency SCs. In another review, the dominance of Si as a PA material was discussed in detail with respect to the increasing proportion of p-Si and m-Si being used for high-efficiency SCs [38]. The economic aspects of the Si solar cell technology in terms of electricity generation, installation, and fabrication etc. were discussed by van der Zwaan and Rabl [39]. The cost-effective testing of Si SCs was suggested by Keogh and Blakers [40], where they carefully measured the cell efficiency under natural sunlight. Apart from this, SCs were also fabricated based on the Si ribbon and Si nanowires [41,42].

2.2 Second generation SC

The research to make the SC technology more economical gave advent to the thin-film-based SCs. Compared to the first-generation SC, the thin-film technology requires remarkably less PA material for almost the same absorption of sunlight [43]. The technology is well established in the market due to its long service life, easy installation, a high flexibility, and a reasonable efficiency of ~12% [44]. The thin-film SCs are manufactured in a one-step process, where a thin-film of PA material is deposited on a transparent conducting substrate.

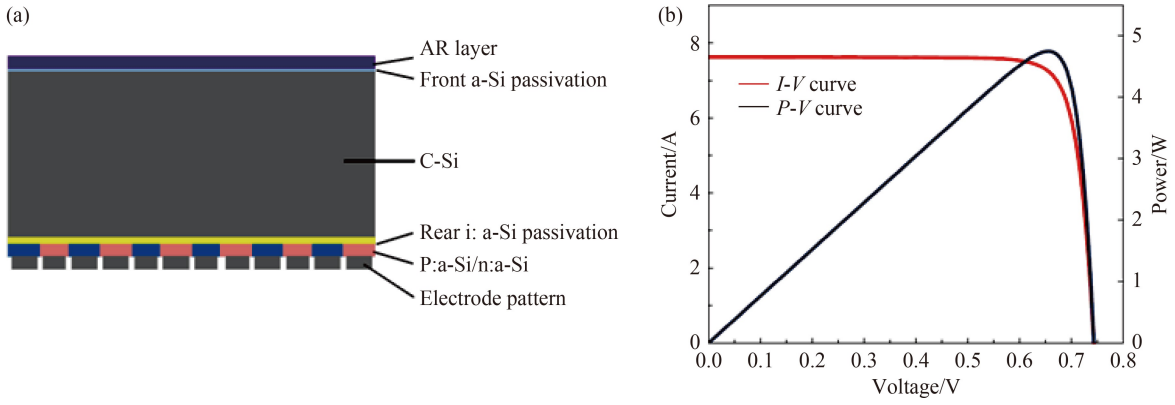

Fig. 2 Heterojunctions and interdigitated back contact-based Si SC.
(a) Schematic of the fabricated device architecture; (b) *I-V* characteristic and power-voltage (*P-V*) curve of the device (180 cm^2 designated area) with PEC of ~26.3% (reprinted with permission from Ref. [29]).

2.2.1 Amorphous/micro-crystalline silicon solar cells

The amorphous/micro-crystalline silicon (a-Si) SC is distinct from the first-generation Si SCs, as it incorporated the thin-film of non-crystalline disordered Si structures, where Si atoms are randomly located with each other. Due to the random arrangement of the atoms, it offers a large band-gap of 1.7 eV [45] and shows a better light absorptivity compared to m-Si [46]. Matsui et al. [47] incorporated hydrogenated a-Si in the improved p-i-n configuration and apprehended an efficiency of 10.22%. Later, Sai et al. [48] applied hydrogenated μc-Si having a layer thickness of ~2 μm, and the fabricated device exhibited an efficiency of 11.9%. The efficiency was further improved by the combined deposition of the a-Si and p-Si on one another. The configuration enhanced the sun light absorption as a thin layer of a-Si on the top which effectively absorbs the shorter wavelengths, and the bottom p-Si layer which effectively absorbs longer wavelengths. Based on the layer thickness and device structure, the efficiency was increased by 8%–9% compared to a-Si SCs.

2.2.2 CdTe/CdS solar cells

The CdTe band-gap is ~1.45 eV, which is nearly an ideal band-gap for improved absorbance in the solar spectrum [49]. This material has a high absorption coefficient, and SCs based on the heterojunction formed between the inherent p-type CdTe and n-type CdS have been reported with an efficiency of ~16.5% [50]. Initially, a thin layer of CdS (~100 nm) is deposited on the transparent conducting substrate, followed by a deposition of CdS, using evaporation processes at a temperature of 400–600 °C [51]. As the materials are inherently doped, no further external doping is required, and deposited films are chemically stable. To improve the quality of the heterojunction, the deposited polycrystalline films are annealed at 400–500 °C in the atmosphere of $CdCl_2$. Though the highest efficiency of the SC is reported as ~16.5%, the commercial module efficiency lies in the range of 10%–11% [50]. The issue is with the back electrical contact, which is compensated by depositing a p^+ layer between the electrode and CdTe [52]. In a recent research, an efficiency of ~21.1% was reported for CdTe-based single-junction SC [53]. The other technical issue is with the use of a toxic Cd environment during the activation step. Moreover, the SC itself is based on the toxic material, and there is a problem with the telluride (Te) raw material. As a result, the technology did not receive much exposure for commercialization and research was focused on the other materials.

2.2.3 Copper indium gallium selenide/copper indium selenide solar cells

In the current scenario, more than 90% of the SC market is based on the c-Si. The cost of production of c-Si based SC is high, and 50% manufacturing cost includes the cost of Si wafer. The sunlight gets efficiently absorbed within the few micron-sized thick Si layer. However, thicker wafers are used in the fabrication process to provide mechanical support, which increases the production cost. In thin-film-based photovoltaics, the a-Si SCs suffer from a lower efficiency of ~12% due to light-induced degradation of material and CdTe SCs are not preferred, as the toxic nature of Te gives concern over their disposal. On the other hand, CIGS thin-film-based SCs seem to be promising candidates to replace c-Si, which also have a comparable efficiency. The CIGS film is deposited on the transparent glass or flexible plastic substrates, which makes them cost-effective and a ~2 μm thick film is sufficient for good absorption of light. As a result, the PA material wastage is low in comparison to the first-generation SCs. However, the increased cost issue can arise with the unstable price of indium once the CIGS SCs are commercialized on a large scale. In the beginning, $CuInSe_2$/CdS (CIS) based photovoltaic cells were synthesized with an efficiency of 4%–5% [54].

Later, by using the co-evaporation deposition technique, Mickelsen and Chen [55] reported the CIS-based SC with an efficiency of 9.4%. Thereafter, various efforts have been made to improve its efficiency, such as introducing Ga in the alloy of CIS material often called $CuIn_{1-x}Ga_xSe_2$ (CIGS), use of thinner CdS layer, sodium doping, and zinc oxide (ZnO) as a buffer layer etc. The CIS has a band-gap of 1.04 eV, and by replacing In with Ga, the bandgap increases up to 1.7 eV [56], which offers a large V_{oc}. The chalcopyrite family includes alloys of Cu(In, Ga, Al)(Se, S)$_2$. Thus, by altering the proportion of Ga/In in the CIGS or S/Se in CIGSSe compound, the bandgap of the PA material can easily be tuned to match the solar spectrum [57]. Apart from being a good light absorber, the other advantages of the CIGS include a high absorption coefficient (10^5 cm^{-1}) and a direct bandgap of 1–1.1 eV [58–65]. For the high efficiency of CIGS SCs, it is desirable to have a Cu/(In + Ga) atomic ratio in the range of 0.88–0.92 and Ga/(Ga + In) as ~0.26 [66,67]. As the Ga atomic ratio increases above 0.3, the defects tend to increase in the film, thereby decreasing the cell efficiency [68]. Over the decades, various deposition techniques and buffer layers have been studied for efficiency improvement [69]. With CdS as a buffer layer, the best result shows an efficiency of 22.6% [70]. Several Cd-free buffer layers like Zn(S, O, OH) [71] and Zn(O, S) [72] (Fig. 3) are pursued in CIGS SC, resulting in an efficiency of ~19.7% and ~18%, respectively. Recently, an efficiency of 22.8% was achieved when a Cd-free buffer layer (Zn, Mg)O/Zn (O, S, OH) was incorporated in the cell [73]. In another study, Cd-free Cu(In, Ga)(Se, S)$_2$(CIGSSe) SCs with $Zn(O, S, OH)_x/Zn_{0.8}Mg_{0.2}O$ double buffer layers exhibited an efficiency of ~23.3% [74]. The theoretical efficiency limit for 1.14 eV bandgap CIGS SC is estimated to be 33.5% [75]. An improvement from the currently reported PCE of 22.8% to 25% is expected in the near future by incorporating approaches like enhancing CIGS absorbance by doping methods, minimizing the defects by surface passivation, using large bandgap Cd-free layers and light-harvesting by redirecting the unused light due to reflection [76].

2.3 Third generation SC

2.3.1 Organic solar cells

Organic SCs (OSCs) are an attractive alternative to the Si-based photovoltaic technology and have been the subject of extensive research over the last decade. The OSCs use organic molecules or conducting polymer as PA materials and are usually flexible. The various advantages of OSCs include high flexibility, lower weight, simple fabrication process, easier integration, etc. The PA material used in the OSC tends to govern the efficiency of the cells. Earlier, the C60 derivative 6,6-phenyl-C61-butyric acid methyl ester (PC61BM), and C70 derivative (PC71BM) were used as acceptors in OSCs. The PA blend of poly(3-hexylthiophene)(P3HT): PC61BM was used by Li et al. [77], and the device responded with an efficiency of 4.4%. The incorporation of thieno-[3,4-b]thiophene (TT) and benzo[1,2-b; 4,5-b′]-dithiophene units in the low bandgap donor PTB1 polymer resulted in an efficiency of 5.6% [78]. In another study, the efficiency of PBDTTT-C-T based SC was improved to 7.59% by conjugating it with the PBDTTT-E-T polymer and attaching functional group to BDT [79]. An efficiency of 9.35% was reported by studying the ITO/ZnO-C60/PTB7-Th:PC71BM/MoO_3/Ag structure in inverted device configuration. Further, the inclusion of dual doping of the ZnO layer in the structure improved the efficiency to 10.31% (see Fig. 4(a)) [80]. The single-junction OSC using PC71BM binary fullerene reached the highest efficiency of 11.7% in 2016 [81]. The use of trialkylsilyl as polymer donor side chains (J71) showed an efficiency of 11.41% [82]. Recently, the use of a non-fullerene acceptor (C8-ITIC) in ITIC showed an increased crystallinity, a high absorption, and the PCE attained the value of 12.4% (see Fig. 4(b)) [83]. In one of the study,

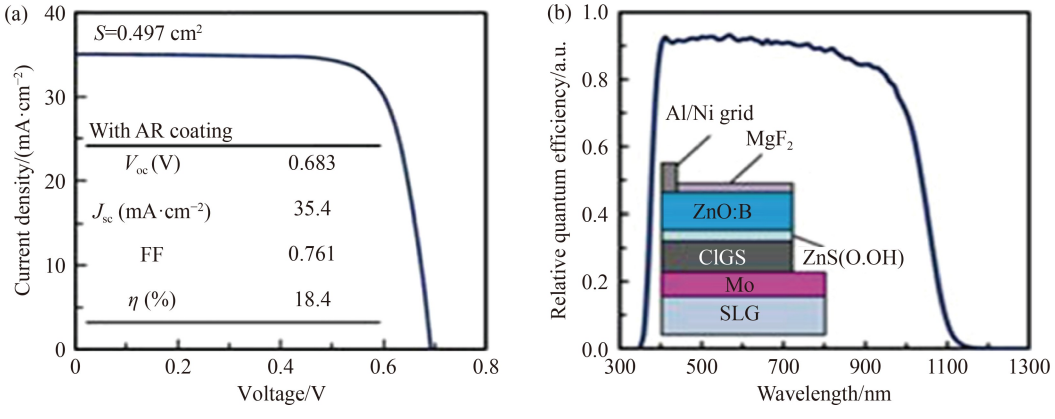

Fig. 3 Photovoltaic performance of second generation SCs.
(a) *J-V* curve; (b) spectral response curve of ZnO:B /ZnS(O, OH)/CIGS based SC (reprinted with permission from Ref. [72]).

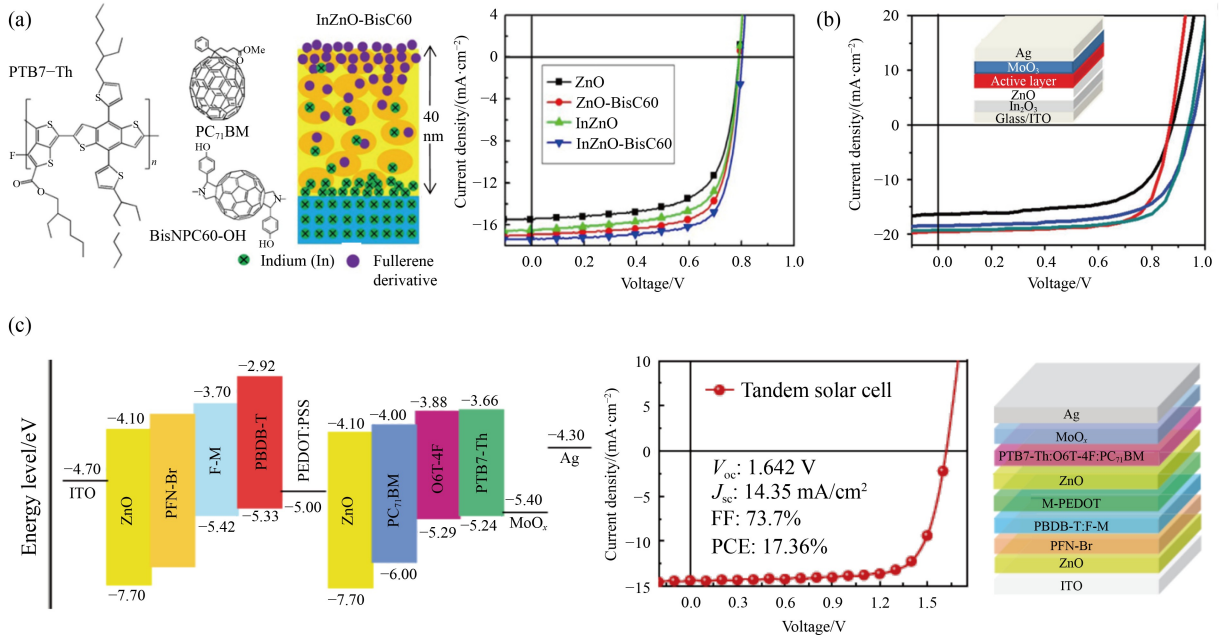

Fig. 4 Photovoltaic performance of OSCs.

(a) Chemical configuration of the materials used for SC fabrication along with a schematic of cathode interlayer and *J-V* curves of the SC ITO/cathode interlayer/PTB7-Th: $PC_{71}BM/MoO_3$/Ag (reprinted with permission from Ref. [80]); (b) *J-V* curve (device structure inset) (reprinted with permission from Ref. [83]); (c) energy level diagram (left), *J-V* plot (middle) and device architecture of tandem OSCs (right) (reprinted with permission from Ref. [86]).

the OSC based on PBDBT-SF:IT-4F resulted in a PCE of 13.1%. The same group synthesized PBDB-T-2Cl polymer, which is a modified version of the polymer used in the previous study by substituting fluorine with chlorine, and the yield of PCE increased to 14% [84]. The PCE of the polymer cells can further be improved by the use of tandem SCs. The tandem cell fabricated by Cui et al. [85] consisted of PTB7-Th:IEICO-4F as bottom cell and J52-2F:IT-M as front cell exhibited an outstanding efficiency of 14.9%. The highest efficiency of ~17.3% was achieved by the tandem OSC fabricated by Meng et al. [86] (see Fig. 4(c)). A detailed review of the PCE of OSCs in terms of various PA materials was done by Xue et al. [87]. di Carlo Rasi and Janssen [88] reviewed the multi-junction OSCs fabricated by the solution-based method. The interfacial processes affecting the performance of OSCs were also reviewed [89].

Non-fullerene acceptors are of tremendous importance in high-efficiency OSCs. Chen and Zhang [90] reviewed the recent progress on non-fullerene small molecule-based acceptor materials and compared their performance in OSCs by using the same donor materials. Chen et al. [91] investigated the performance of perylenediiimide (PDI) based acceptor materials in solution-processed OSCs. The PCE of the fabricated device reached up to 2.73% which demonstrates that the 3D structural design of acceptors can be an effective way to improve the performance of fullerene-free OSCs. In another work, Sun et al. [92] successfully synthesized a novel PDI-small molecule acceptor by fusing PDI units and a spiro core 4,4′-spirobi[cyclopenta[2,1-b; 3,4-b′] dithiophene] (SCPDT) via β-position coupling with thiophene bridges. The OSCs fabricated using SCPDT based molecules as acceptors and PTB7-Th as donors were demonstrated to show an excellent performance with a PCE as high as 8.89%. Li et al. [93] designed and synthesized non-fullerene acceptors with branched side chains and improved molecular packing for OSCs applications. The acceptors were designed by replacing the beta position of the thiophene unit on a Y6-based diethienothiophen [3,2-b]-pyrrolobenzothioadiazole core with branched alkyl chains. Such modifications to the different alkyl chains lead to the change in the molecular packing behavior of non-fullerene acceptors, thereby improving the structure order and charge transport in thin films. They developed a series of non-fullerene acceptors, L8-R (with R as the alkyl chain). The single-junction OSCs based on L8-BO (2-butyloctyl substitution) combined with polymer donor PM6 yielded a high PCE of 18.32%, with a low E_{loss} of 0.55 eV and a high fill factor of 81.5%. The high PCE and fill factor suggest that optimizing morphology and the modification of electronic structure is a feasible option for enhancing the performance of solution-processed OSCs.

2.3.2 Dye-sensitized solar cells

The dye-sensitized solar cells (DSSCs) have a unique way of harvesting solar energy and convert into electrical

energy. Compared to other SC technologies, the DSSCs use dyes that govern the light absorption, charge generation, and charge carrier injection into the semiconductor. The concept of DSSC originated in 1991 when O'Regan and Grätzel [94] demonstrated that incorporating mesoporous metal oxides framework could result in efficient PCEs. The classical device structure of DSSC is shown in Fig. 5(a). The device structure consists of two conducting sheets, one being the working electrode or photo electrode, and the other, a counter electrode. The working electrode usually has n-type ZnO, TiO_2, Nb_2O_5, and SnO_2 deposited on the ITO/FTO substrate [95]. These layers are often called blocking layers, as they avoid direct contact with an electrode. The redox electrolyte is responsible for the regeneration of the oxidized dye and charge transport between the electrodes. The other device structure is called solid-state DSSCs (ssDSSCs). In ssDSSCs, the liquid electrolyte junction is replaced by a solid redox hole transport material, which makes contact with the electrode and forms an intercalated network with the mesoporous TiO_2. The efficiency of the DSSCs mainly depends on the performance of the dye used in the SC. The dye should be able to absorb the light from UV to the visible region. It should firmly be grafted on the surface of the semiconductor. Moreover, its HOMO should be more positive than the redox potential of the electrolyte, and the LUMO has to be more negative than the conduction band of the semiconductor and should be stable to sustain at least ~10^8 redox turnovers which correspond to about 20 years of cell operation [96]. The various dye sensitizer incorporated in the DSSCs can be classified as metal complex, metal-free, and natural sensitizers [97,98]. The electrolyte in the DSSCs helps in the regeneration of the dye and transport of the charge carrier; thus, it determines the stability and functionality of the SC over the period of time. The electrolyte must be highly conducting, should not degrade the dye or assist desorption of dye from the semiconductor surface, and must establish a good interfacial contact with the electrode and semiconductor oxide. The various electrolytes used are liquid, organic, ionic, and solid-state electrolytes [99,100]. An efficiency of 6.17% was achieved by using 3-D hybrid material comprising of TiO_2 nanotubes (NTs) array filled with CNT-G-TiO_2 nano-paste as a photoanode [101]. Qiu et al. [102] demonstrated an enhancement in efficiency by modifying the photoanode with different size nano-spindle anatase TiO_2. They reported a two-layer structure with variable size. The single crystalline TiO_2 nano-spindles exhibited an efficiency of 8.3% (see Fig. 5(b)). Maheswari and Venkatachalam [103] deposited a photo-anode with composite of TiO_2 nanowires (TNPWs) as the base material and zirconia as the doping metal. Hafnium oxide (HfO_2) was applied on the zirconia doped TNPWs (zirconia/TNPWs) film and served as a blocking layer. The fabricated DSSC SC with zirconia/TNPWs doped photo-anode and blocking layer revealed an efficiency of 9.93%. Recently, an efficiency of 10.3% was reported by Huang et al. [104] by incorporating a single-layer film of mesoporous TiO_2 resulting in outstanding dye loading and light scattering abilities as well as attenuated charge recombination (see Fig. 5(c)). Furthermore, they reported that an impressive efficiency of 11.2% can be obtained after $TiCl_4$ post-treatment. The highest efficiency of 12.3% was reported for cobalt(II/III) based redox electrolytes [105].

In another study, a PCE of 1.37% was reported using a pair of carbon-based electrodes [106]. The conducting carbon nanotubes (CNTs) films were modified with titanium sub-oxide (TiO_x) and used as working electrodes. Further, a bilayer of CNTs and carbon black was used as a counter electrode. The modification of the working electrode using TiO_x enhances the performance of the device. Moreover, the device performance was further improved when carbon black was included in the counter electrode. The efficiency enhancement was attributed to the restriction of mass recombination by TiO_x at the interface between electrode/electrolyte and the acceleration of the electron transfer kinetics by carbon black at the counter electrode. The same group of researchers reported a PCE of 1.8% for DSSC fabricated using transparent electrodes based on TiO_x modified CNT [107]. They demonstrated that the TiO_x modified CNT film served as a potential window electrode for liquid-type DSSCs [107]. Tantang et al. [108] fabricated nitrogen-doped CNT-based bilayer thin films as transparent counter electrodes for DSSCs and achieved a PCE of 2.18% and a transmittance of ~57% at 550 nm. The fabricated DSSC device consisted of FTO/TiO_2 as working electrode and bilayer CNT films as counter electrodes (Fig. 6). They demonstrated that the DSSCs with bilayer CNT-based transparent electrodes significantly improved performance compared with normal CNT-based counter electrodes. Moreover, the solar cell device with transparent bilayer counter electrodes was found to harvest energy at back illumination, which meant that the light was back-illuminated via diffuse reflections of sunlight.

2.3.3 Perovskite solar cells

The typical perovskite structure is an organic-inorganic hybrid with a formula ABX_3, where A is a monovalent cation (e.g., rubidium (Rb), cesium (Cs), formamidinium (FA), and methyl ammonium (MA)), B is a divalent cation (e.g., Tin (Sn) and lead (Pb)), and X is a halide (e.g., bromine (Br), chlorine (Cl) and iodine (I)) [109,110]. The PSCs efficiency was improved from ~3.8% [111] to

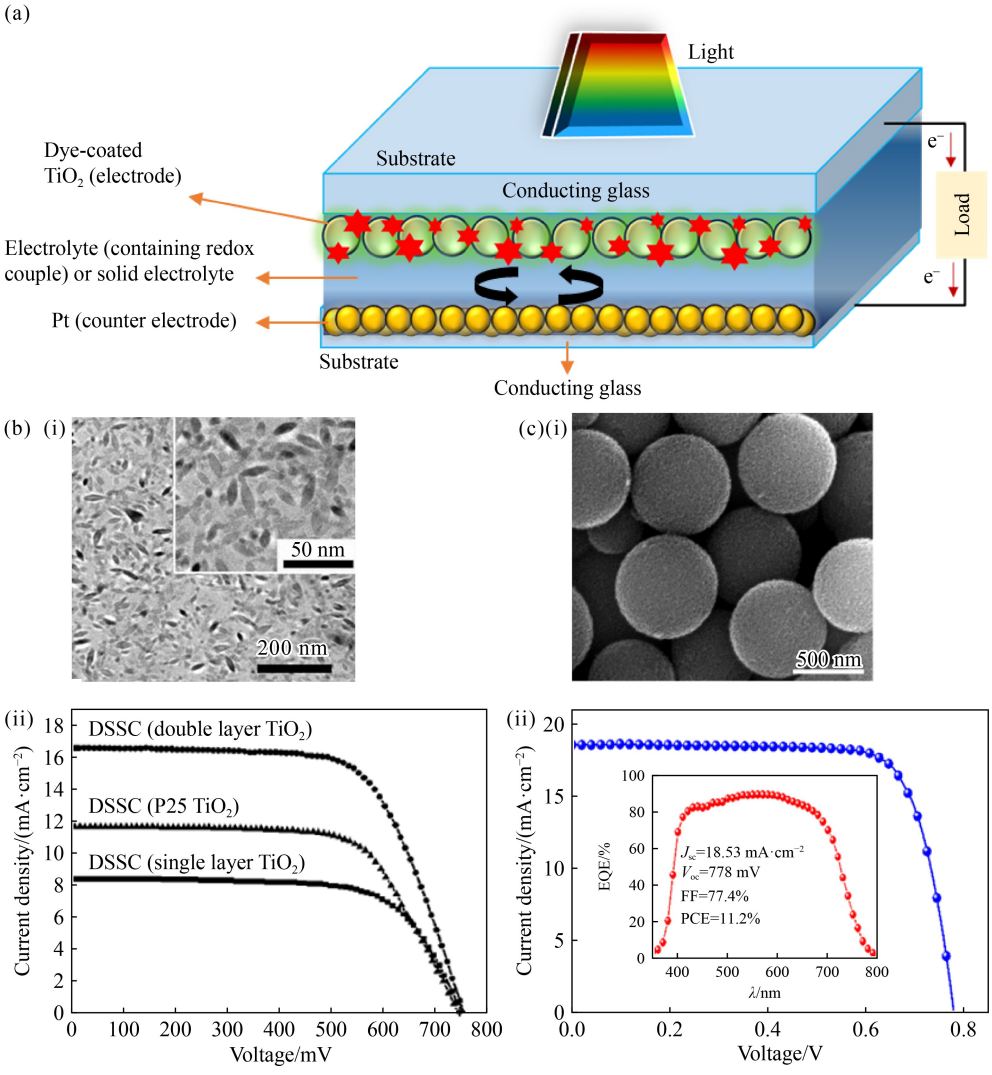

Fig. 5 Photovoltaic performance of the DSSCs.

(a) Device configuration of conventional DSSC; (b) DSSC is based on double-layer TiO_2 nano-spindles: (i) SEM image of synthesized large and small TiO_2 nano-spindles, (ii) *J-V* plot of fabricated DSSCs incorporating single and double layers of large and small nano-spindles (reprinted with permission from Ref. [102]); (c) TiO_2 sphere photoanode incorporating DSSC: (i) FESEM and TEM image TiO_2 spheres, (ii) *J-V* curve and EQE curve of fabricated DSSC (reprinted with permission from Ref. [104]).

~24.8% [112] with a time scale of 2009 to 2020, respectively (see Fig. 7(a)). This speedy improvement in the efficiency of the PSCs is due to unique properties such as direct bandgap (~1.5 eV), high carrier mobility, charge diffusion length of 100–1000 nm and high absorption coefficient. The PSCs are classified into two types of structures i.e., p-i-n and n-i-p device configurations. The p-i-n configuration is based on the OSCs and consists of the ITO/hole transport layer (HTL, p-type)/perovskite/electron transport layer (ETL, n-type)/metal electrode [113,114]. On the other hand, the n-i-p configuration is based on the DSSCs and consists of the FTO/(ETL, n-type)/perovskite/(HTL, p-type)/metal electrode [115,116]. The n-type SnO_2, ZrO_2, ZnO, Al_2O_3, and TiO_2 etc., are chosen as ETL materials due to the suitable band alignment with the perovskite material [117]. The PSCs are synthesized by the solution-based methods at a lower processing temperature of ~150°C and can form high-quality crystalline films [118]. Moreover, based on the nature of the halogen in the perovskite, the energy bandgap can be tuned from 1.5 to 2.3 eV. This bandgap engineering is found to be more effective for $CH_3NH_3Pb(I_{3-x}Br_x)_3$ perovskites [119]. An efficiency of 3.8% was reported in 2009 using $CH_3NH_3PbBr_3$ and $CH_3NH_3PbI_3$ nano-crystals with TiO_2 as ETL [111]. In 2011, with a systematic study of the perovskite, the efficiency was improved to 6.5% [120]. Further, an efficiency of 9.7% was reported by employing spiro-MeOTAD as HTL and $CH_3NH_3PbI_3$ as the perovskite material [121]. The mixed halide perovskite was studied in a porous alumina template, and the reported efficiency was 10.9% [122]. Along with the mixed halide when graphene was

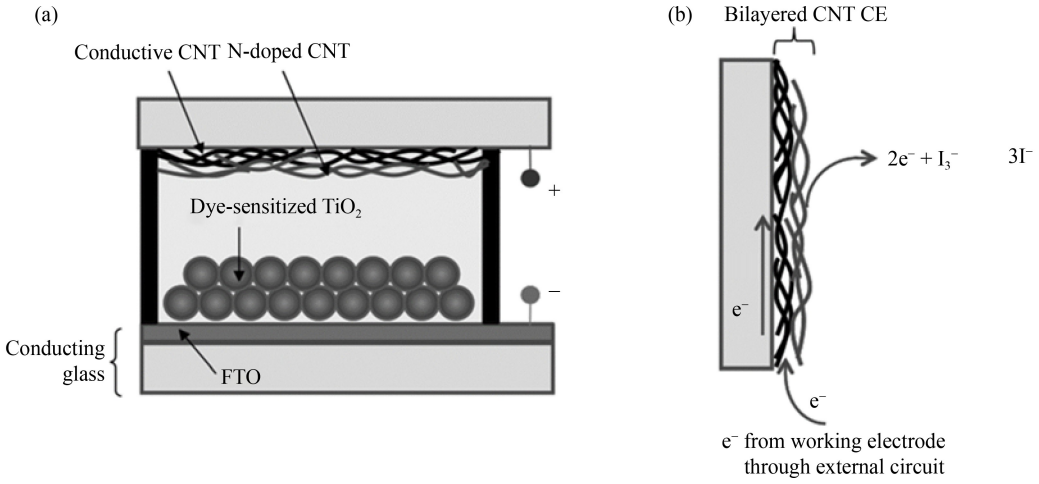

Fig. 6 Nitrogen-doped CNT-based bilayer counter electrode for DSSC.

(a) Schematic illustration of a DSSC with a bilayer CNT-based transparent counter electrode; (b) representation of electron transport along with a normal conducting CNT film and injection of electrons back to the electrolyte via the redox reaction between N-doped CNT and redox species (reprinted with permission from Ref. [108]).

incorporated, it resulted in an enhanced charge collection and an efficiency reached 15.6% (see Fig. 7(b)) [123]. In another study from $CH_3NH_3PbI_3$ perovskite, an efficiency of 15.7% was reported using ZnO as the photo-cathode [124]. To further improve the perovskites properties and photovoltaic performance, efforts were made to partially replace the Pb^{2+} ions in the B-site with metal ions. These studies revealed that the incorporation of particular heterovalent metal ions, in turn, affects the crystallographic and optoelectronic properties of perovskite films. However, the influence of the partial replacement of Pb^{2+} ions with alternative metal species at the B-site on the properties and photovoltaic performance of the materials still remains unclear [125]. For example, experimental studies demonstrated that the partial replacement of Pb with several alternative divalent metal species such as Co, Cu, Fe, Mg, Mn, Ni, Sn, Sr, and Zn affects the photovoltaic performance and optical properties of methylammonium lead triiodide perovskite films [125]. The perovskite film was found to be tolerant to most of the homovalent metal species and the combination of Pb-Co in the mixed metal perovskite resulted in the highest PCEs with only 6% Pb^{2+} replacement [125]. Another study indicated that the incorporation of Bi^{3+} into $MAPbBr_3$ led to the reduction in the bandgap and the enhancement in the conductivity via electronic doping [126] while In^{3+} and alkali metals such as Na^+ and K^+ affected the morphology and crystallinity of $MAPbI_3$ [127,128]. Similarly, the incorporation of Al^{3+} led to the reduction in the nonradioactive recombination rate and improved crystal quality by reducing the microstrain in the $MAPbI_3$ lattice [129]. However, very few reports are available on the homovalent Pb^{2+} substitution. For example, van der Stam et al. [130] reported a post synthesis cation exchange method that allowed the partial substitution of Pb^{2+} with other divalent cations such as Sn^{2+}, Cd^{2+} and Zn^{2+} that resulted in the blue shift of photoluminisence (PL) bands, narrow emission bandwidth, high PLQYs, and sharp absorption transitions. Kour et al. [131] demonstrated that the divalent cations of alkaline earth metals such as Mg^{2+}, Ca^{2+} and Sr^{2+} can be effectively used as a substitute for Pb^{2+}. Several researchers suggested that Sn^{2+} could also be used to replace some portion of Pb^{2+} at the B-sites resulting in the reduction of bandgap [132–134]. However, one of the main drawbacks of Sn^{2+} is that it gets oxidized to Sn^{4+} readily when exposed to air, thereby causing destabilization of perovskite into multiple phases and subsequently reducing the photovoltaic performance [125]. Moreover, it was shown that Sn-based perovskites are toxic in nature and they pose serious health issues due to environmental acidification caused by degradation [135]. Thus, finding an alternative divalent metal species capable of tuning the optoelectronic properties of perovskites without damaging the stability and without intensifying the toxicity of the inherent materials remains an attractive pursuit. Recently, Zn(II) received much attention due to its considerable stability resulted in dense and smooth films with reduced pinhole defects. Kooijman et al. [136] reviewed the stabilization of the perovskite film with Zn(II) doping and its role in improving the efficiency of the PSC. An efficiency of 16.3% and 18.35% was reported by including 0.1% and 3% Zn(II) in the film, respectively [137,138]. With the incorporation of different concentrations of Zn^{2+} ion, the quality of the target film was improved with a lesser trap state density and a bigger grain size (Fig. 7(c)). Various research groups improved the efficiency to ~20% by incorporating 1% Zn(II) [139]. Jung et al. [140] used P3HT as an HTM

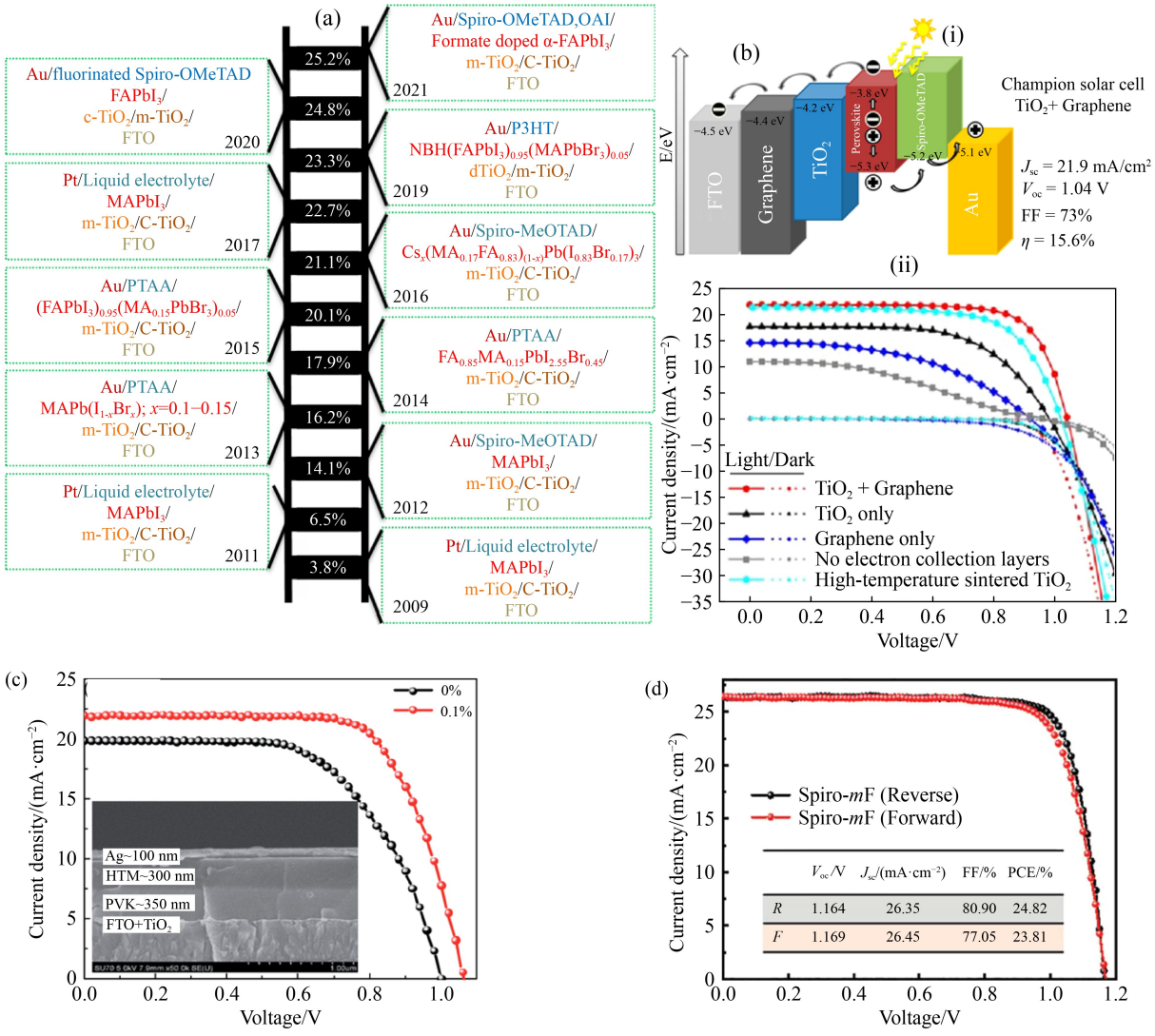

Fig. 7 Photovoltaic performance of PSCs.

(a) Schematic illustrating an improvement in the efficiency of PSCs with respect to timescale; (b) (i) schematic representing of energy levels of the elements used in the fabrication of SC along with electrical parameters of champion SC (TiO_2 + graphene), (ii) comparison of *J-V* cure of SC fabricated by varying the device configuration (reprinted with permission from Ref. [123]); (c) *J-V* characteristics 0.1% Zn^{2+} doped PSC and inset show the cross-sectional SEM image of the fabricated SC (reprinted with permission from Ref. [137]); (d) *J-V* curves of the best performing SC fabricated by incorporating fluorinated Spiro-OMeTAD as HTM (reprinted with permission from Ref. [112]).

without any dopants in the device architecture. A thin layer of wide bandgap halide perovskite is formed on the top of the narrow bandgap light perovskite layer by an *in situ* reaction of n-hexyl trimethyl ammonium bromide. The best device with configuration of FTO/$dTiO_2$/mp-TiO_2/$NBH(FAPbI_3)_{0.95}(MAPbBr_3)_{0.05}$/P3HT/Au displayed an efficiency of 23.3%. Jeong et al. [112] developed fluorinated isomeric analogs of Spiro-OMeTAD to improve the non-covalent interaction and conjugate energy levels. The synthesized spiro-OMeTAD was used as HTM in SC, and the champion cell exhibited an efficiency of 24.82% (see Fig. 7(d)).

In the last decade, the PSCs technology witnessed tremendous growth as a next-generation SCs for practical applications because of their low cost and facile fabrication process and enhanced PCEs. However, there is still a huge scope to improve the efficiency of PSCs by systematic material composition and device engineering [141,142]. Gu et al. [142] developed an Azacene derivative (QCAPZ) as a promising electron transport layer for inverted PSCs through solution processing without adding any dopants or additives. Figure 8(a) shows the structure of an inverted PSC device fabricated using QCAPZ as an electron transport layer. Figure 8(b) shows the optimized current density-voltage curve of the fabricated PSC device. The fabricated inverted PSC displayed a PCE as high as 10.26% with a current density of 16.55 mA/cm^2, an open-circuit voltage of 0.86 V, and a fill factor of 72.1%. Figure 8(c) displays the incident photon-to-electron conversion efficiency (IPCE)

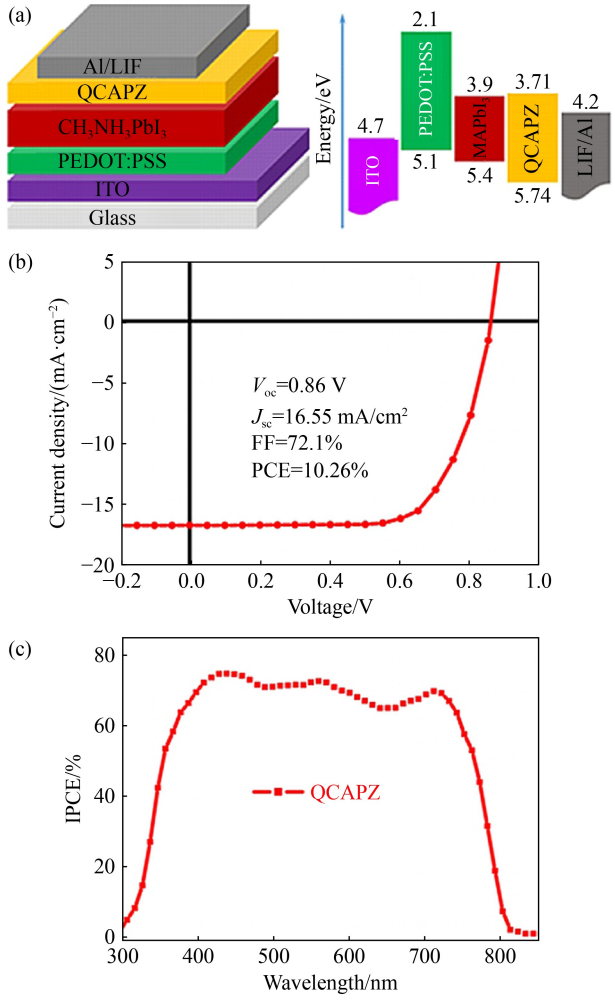

Fig. 8 Azaacene derivative-based electron transport layer in inverted PSC.

(a) Device structure and corresponding energy level; (b) photovoltaic performance of PSC device; (c) Incident photon-to-electron conversion (IPCE) efficiency response of the device (reprinted with permission from Ref. [142]).

spectrum of the PSC device. The maximum absorption was observed to be ~450 nm and a reduction in IPCE in the short-wavelength region that can likely be attributed to parasitic absorption in ITO. Moreover, the integrated current density for the fabricated device was 16.7 mA/cm^2, which was in good agreement with the measured value of 16.55 mA/cm^2. In another report [143], the same group of researcher demonstrated a new sulfur-containing azaacene (TDTP) small molecule as an electron transport layer to improve the performance of metal oxide-free solution-processed PSCs. The inverted PSC device based on sulfur-containing azaacene shows a PCE of 18.2%, which is higher than non-sulfur containing azacene (PYPH) [143]. This superior performance can be attributed to the strong interaction between TDTP and the perovskite surface than that between PYPH and the perovskite surface. These results suggest that simple n-type sulfur containing small molecules can be a promising electron transport layer for further development and practical applications of inverted PSCs [143].

Recently, Jeong et al. [144] introduced an anion engineering concept where pseudo-halide anion formate ($HCOO^-$) was used to suppress anion vacancy defects presented at the grain boundaries and on the surface of the solar cell films. This method is an easy route to remove the lattice defects present in metal halide perovskites, and it also provides easy access to the solution-processed films with an enhanced performance. The PSC device was fabricated using formamidinium lead triiodide ($FAPbI_3$) in a configuration as shown in Fig. 9(a). The *J-V* curves of the reference and target PSCs are depicted in Fig. 9(b). The reference cell attained a PCE of 23.92%, a J_{sc} of 25.72 mA/cm^2, a V_{oc} of 1.153 V, and an FF of 80.69. On the other hand, the target PSC attained a maximum PCE of 25.59%, a J_{sc} of 26.35 mA/cm^2, a V_{oc} of 1.189 V, and an FF of 81.7%. Figure 9(c) shows the statistical distribution of the measured PCEs of the reference and target PSCs. The external quantum efficiency (EQE) of the reference cell was lower than that of the target cell within the whole visible light region (Fig. 9(d)) [144]. The EQE_{EL} of the PSCs is shown in Fig. 9(e) with values of 2.2% and 10.1% for reference and target cell with respective injection current densities of 25.5 mA/cm^2 and 26.5 mA/cm^2, respectively. Figure 9(f) shows the linear relationship between V_{oc} and the logarithm of light intensity. The ideality factor (η_{id}) of the reference and the target cell was 1.18 and 1.52, respectively. Furthermore, the $FAPbI_3$ based PSCs attained a PCE of 25.6% with an operational stability of 450 h [144].

2.3.4 Multi-junction/tandem solar cells

The prime focus in the SC is to efficiently absorb the complete solar spectrum radiation, resulting in the generation of the charge carriers and thereby increasing the PCE of the device. This is practically not possible by a single PA material in a single p-n junction device. Thus, to increase the solar spectrum absorbance, different PA materials are combined, forming multiple p-n junctions, and each material responds to a different range of wavelengths for generating electricity. The layer thickness and bandgap of materials are tuned to achieve current matching. The cells are usually series-connected using a tunnel junction and monolithically integrated [145]. Guha [146] reported the efficiency of the single, double, and triple junction as 9.3%, 12.4%, and 13%, respectively. The multi-junction SCs efficiency status was reviewed by Yamaguchi et al. [147]. Takamoto et al. [148] reported InGaP/GaAs/InGaAs based triple junction SCs with a high efficiency of 44.4% by inverted lattice mismatch fabrication procedure. In another study, Dimroth et al. [149] adopted the wafer bonding method

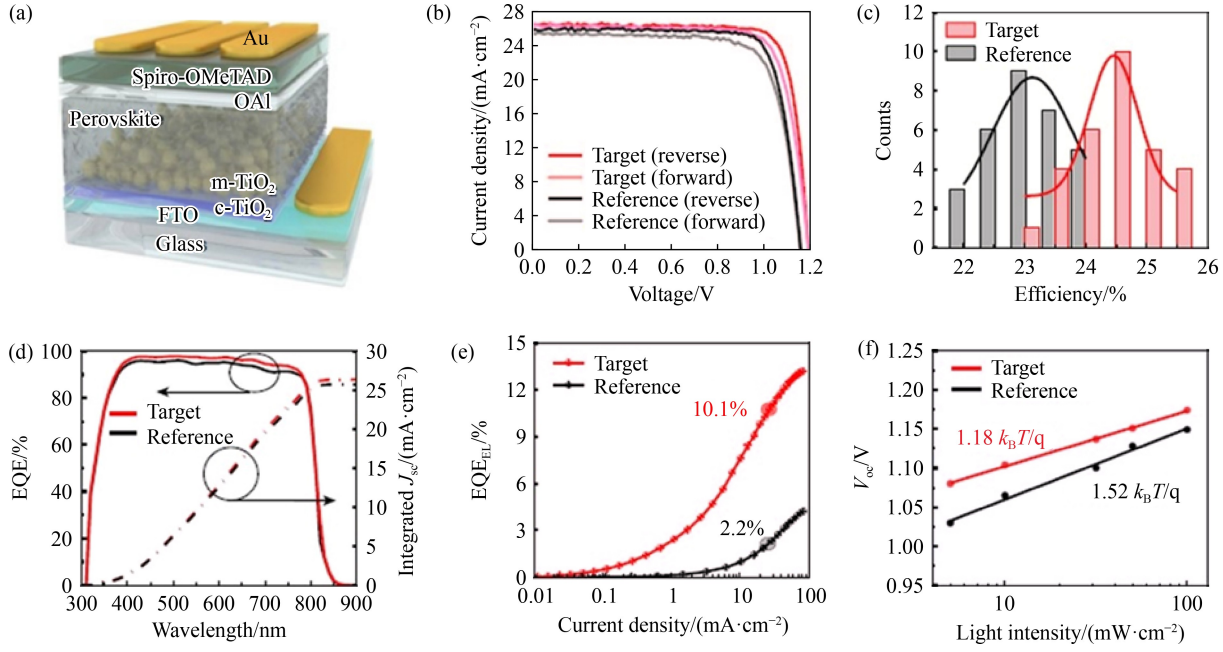

Fig. 9 Pseudo-halide anion engineering based α-$FAPbI_3$ PSC.

(a) Configuration of $FAPbI_3$ based PSC device; (b) *J-V* curves of target and reference cells with respect to forward to reverse voltage scans; (c) distribution of the measured PCEs of PSCs; (d) EQE and the integrated J_{sc} of PSCs; (e) EQE_{EL} measurements of PSCs under current densities of 0.01 mA/cm^2 to 100 mA/cm^2; (f) relation between V_{oc} and light intensity of PSCs (reprinted with permission from Ref. [144]).

to combine III-V compound materials to apprehend the best possible material properties for multi-junction SCs. They demonstrated an efficiency of up to 46.1% for a wafer bonded GaInP/GaAs//GaInAsP/GaInAs grown on InP engineered substrate. Geisz et al. [150] proposed strategies for practical six junctions (AlGaInP/AlGaAs/GaAs/GaInAs) inverted metamorphic multi-junction concentrator SC designs with the potential to exceed 50% efficiency using moderately high-quality junction materials.

Crystalline Si SCs dominate the current photovoltaic market because of their high efficiency and well-established fabrication techniques [151,152]. The present record PCE of crystalline silicon SCs is 26.7%, which is close to their intrinsic limit (29.1%) [29,153]. Recently, Si-perovskite tandem SCs have attracted worldwide attention. SCs fabricated with two semiconductors having different bandgaps can be beneficial in attaining higher efficiencies when utilized in tandem than as individual SCs. The conventional silicon SCs primarily convert the infrared components of light efficiently into electrical energy, while certain perovskites can effectively utilize the visible components of sunlight, making this a powerful combination. Furthermore, the tuned bandgap of perovskites provides an opportunity for the fabrication of Si-perovskite SCs with a tremendous potential of enhancing the intrinsic PCEs of each subcell. In tandem cells, the high transparency and good conductivity of the top electrode of the top cell are the two key factors [154]. Si heterojunction cells have a high efficiency and an ideal bandgap; therefore, it would be interesting to combine Si heterojunction bottom cells and perovskite top cells. Besides, Si-perovskite tandem cells offer an easy way to fabricate high-efficiency SCs without affecting the fabrication cost [154]. Recently, Al-Ashouri et al. [155] reported Si-perovskite tandem SCs with a PCE greater than 29%. Moreover, Si-perovskite tandem SCs demonstrated an improved stability and compatibility when textured Si substrates were used [156–158]. However, the practical limit for all these tandem SCs is over 30% which indicates that these SCs still have some room for improvement [155]. Figure 10(a) demonstrates the mechanically stacked device structure of Si-perovskite SCs where perovskite top cell is used to absorb short-wavelength photons while the Si heterojunction as the bottom cell is used to capture the sunlight in the near-infrared region [154]. The efficiency of Si-perovskite tandem SCs was calculated by testing Si bottom cell filtered by perovskite top cell. Figure 10(b) depicts *J-V* curves of different SCs. The pristine Si heterojunction SC attained a PCE of 23.4% with a V_{oc} of 708 mV, a J_{sc} of 40.1 mA/cm^2, and a fill factor of 82.5%. The filtered Si bottom cell attained a PCE of 8.5% with a V_{oc} of 698 mV, a J_{sc} of 14.5 mA/cm^2, and a fill factor of 83.5%. Figure 10(c) demonstrates the EQE of perovskite top and Si bottom cells. The photocurrent densities of perovskite top and Si bottom cells are 21.3 mA/cm^2 and 14.1 mA/cm^2, respectively. For the perovskite top cell, the EQE in the wavelength range of 500–820 nm showed a decreasing trend, while for the Si bottom cell, a response was observed around 500 nm. These results were in good agreement with the transmittance

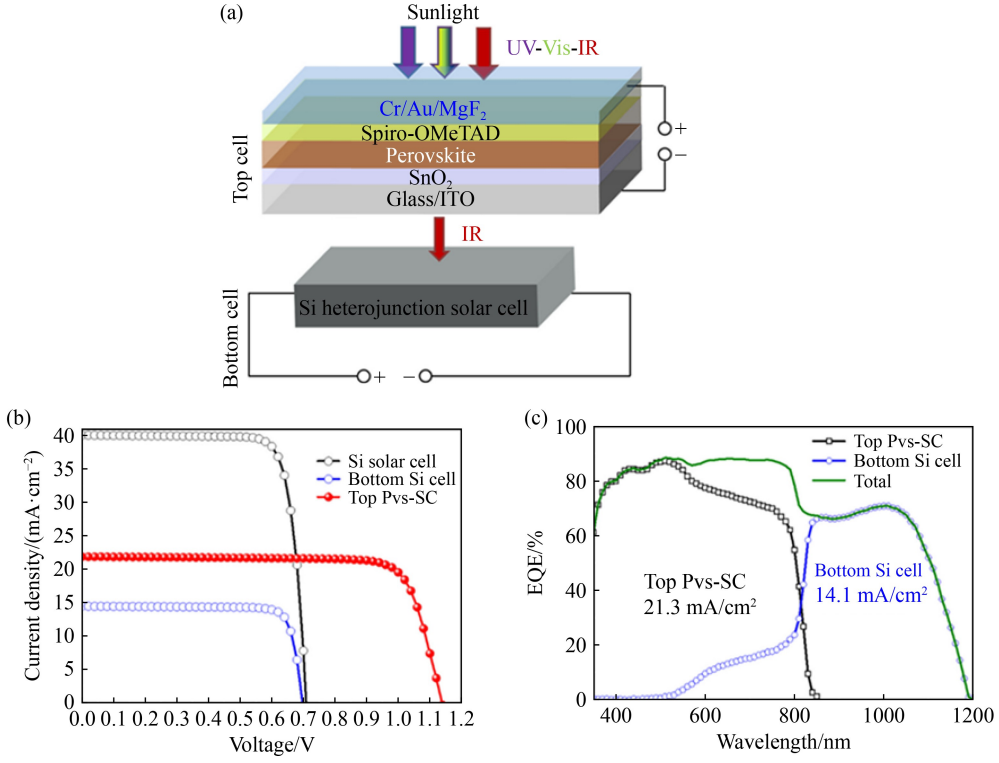

Fig. 10 Device performance of Si-perovskite tandem SC.
(a) Si-perovskite device architecture; (b) *J-V* curves; (c) EQE for different SCs (reprinted with permission from Ref. [154]).

characteristics of the perovskite device. The reduced V_{oc} of the filtered Si cell was attributed to the low intensity of sunlight in the Si bottom cell than in the original Si device [159]. Moreover, the high fill factor of the Si bottom cell is attributed to the low photon-induced charge carrier concentration resulting from the relatively fewer photons within the filtered Si SC [160]. Table 1 illustrates the photovoltaic parameters of a few high-performance SCs reported to date.

3 Recent advances in SC fabricated by popular scalable solution deposition methods

3.1 Spray coating

Spray coating is a solution-based process in which a liquid precursor is mechanically forced by a carrier gas toward the target surface and deposits a thin film of liquid. The atomization is generated by different ways like cavitation of the precursor, ultrasonic simulation, and flow rate of carrier gas. Compared to other spray coating techniques, ultrasonic spray coaters have a more precise control over airflow, droplet size and spray cone. The main drawback of spray coating is the inhomogeneity and quality of the layers, with respect to those produced by standard reference techniques such as spin coating. In addition, the quality of the ink atomization is the main factor that affects the homogeneity of the film. The SCs fabricated using spray coating usually have lower efficiencies than those fabricated by spin coating and similar laboratory-scale methods. The spray coating of OSC was first reported in 2007 by Vak et al. [161], where the PA layer of P3HT:PCBM was spray-coated, and the fabricated device showed an efficiency of 2.83%. In 2009, Hoth et al. [162] demonstrated the multilayer spray coating of PA P3HT:PCBM layer with PEDOT:PSS as HTL, and the device apprehended a PCE of 2.7%. It was found that the topography of the spray-coated films depends on the selection of the solvent. Considering this, a mixed solvent was used by Girotto et al. [163], and a PCE of 3.75% was achieved. This study highlighted the improvement in the surface coverage of the film by the mixed solvent system. In another work, the HTL, ETL, and PA layer, i.e., PEDOT:PSS, ZnO, and P3HT:PCBM, were deposited by spray coating, and the devices exhibited a PCE of 3.17% with an active area of 0.36 cm [164]. Further, an efficiency of 5% was reported by Wang et al. [165]. Later, a PCE of 8.06% was reported by spray coating PBDTTT-EFT:$PC_{71}BM$ film and PEDOT:PSS on a large-area substrate (25 cm^2) with an active area of 6.45 mm^2 (see Fig. 11(a)) [166]. The introduction of the perovskite material made a mark in solar technology, and several studies were reported on spray-coated PSCs. For the first time, the ultrasonic spray coater was used by Barrows et al. [167] to deposit the precursor solution of $CH_3NH_3PbI_{3-x}Cl_x$. The study revealed that to minimize

Table 1 Photovoltaic parameters of high-performance SCs reported in the literature

Material	J_{sc} /(mA·cm^{-2})	V_{oc} /V	FF/%	Efficiency/%	Ref.
m-Si	42.3	0.744	83.8	26.3±0.5	[29]
a-Si	16.36	89.6	69.8	10.22±0.3	[47]
μc-Si	41.14	0.711	79.3	23.2±0.3	[48]
CdTe	31.69	0.887	78.5	22.1±0.5	[53]
ZnS(O,OH)/Cu(In,Ga)Se_2 (CIGS thin-film)	35.4	0.683	76.1	18.4	[72]
CIGS (thin film)	39.4	0.721	78	22.3	[73]
CIGS (Cd-free) with Zn(O,S,OH)$_x$/$Zn_{0.8}Mg_{0.2}O$ buffer layer	39.58	0.73	80.4	23.35±0.5	[74]
OSC (thin film)	17.24	0.8	74.1	10.31	[80]
OSC (thin film)	19.8	0.78	73	11.7	[81]
OSC (thin film)	17.4	0.94	68	11.20±29	[82]
OSC (thin film)	19.3	0.93	69	12.4±0.4	[83]
OSC (thin film)	12.8	0.86	77	14	[84]
OSC (thin film)	13.3	1.65	68	14.9	[85]
OSC (thin film)	14.32	1.636	72	17.36	[86]
DSSC	17.16	0.65	55	16.7	[97]
DSSC	16.4	0.76	66.8	8.3	[98]
DSSC (TNPWs/ZrO_2/HfO_2)	20	0.73	68	9.93	[99]
DSSC	17.38	0.77	76.6	10.3	[100]
DSSC	17.66	0.93	74	12.3	[101]
FTO/graphene/TiO_2/$CH_3NH_3PbI_{3-x}Cl_x$/spiro-OMeTAD/Au	21.9	1.04	73	15.6	[123]
FTO/TiO_2/$CH_3NH_3Pb_{1-x}Zn_xI_{3-y}Cl_y$/ spiro-OMeTAD/Ag	21.98	1.06	70	16.3	[137]
FTO/dTiO$_2$/mp-TiO_2/NBH$(FAPbI_3)_{0.95}(MAPbBr_3)_{0.05}$/ P3HT/Au	24.88	1.15	81.4	23.3	[140]
FTO/TiO_2/$FAPbI_3$/fluorinated spiro-OMeTAD/Au	26.35	1.16	80.9	24.28	[112]
InGaP/GaAs/InGaAs	–	–	–	44.4±2.6	[148]
GaInP/GaAs/GaInAsP/GaInAs				46±2.2	[149]
AlGaInP/AlGaAs/GaAs/GaInAs	–	–	–	47.1±2.6	[150]

the pinholes and improve the film uniformity, it is necessary to control the drying rate of the film. The fabricated device in an inverted configuration of ITO/PEDOT:PSS/Perovskite/PCBM/Ca/Al displayed an efficiency of 11% (see Fig. 11(b)). In a similar study, the device configuration of FTO/compact TiO_2/Perovskite/Spiro-OMeTAD/Au fabricated by Das et al. [168] exhibited a PCE of 13% (see Fig. 11(c)). Further, Tait et al. [169] reported an efficiency of 15.7% for small-scale devices and 11.7% for 3.8 cm^2 area modules using spray coating of lead acetate perovskite precursor (see Fig. 11(d)). An efficiency of 16.03% was obtained from $CH_3NH_3PbI_3$ PSC by the two-step spray coating method, and a scale-up device of 1 cm^2 area displayed an efficiency of 13.09% (see Fig. 11(e)) [170]. In another study, Heo et al. [171] made a slight modification in the technique, where they balanced the incoming flux of the precursor with the outgoing flux of evaporating solvent. The champion cell fabricated using this technique achieved an efficiency of 17.8% (forward scan), 18.3% (reverse scan), and (16.08±1.28%) (average) for unit cells under 1 Sun condition (see Fig. 11(f)). The commercial acceptance of the technology will be there if all the layers of the SC can be deposited by spray coating under ambient conditions. Mohamad et al. [172] demonstrated this in 2016, where they spray-coated PEDOT:PSS, $CH_3NH_3PbI_{3-x}Cl_x$, and PCBM and reported an inverted configuration based device with the highest and average efficiency of 9.9% and (7.1±1.7%), respectively. Using a normal device configuration of FTO/TiO_2(compact)/TiO_2 (mesoporous)/perovskite/spiro-OMeTAD/Au, Bishop et al. [173] reported an efficiency of (9.2±0.6%). Thus, in the future, an efficiency of 18% is expected to be attained using the spray coating technique. However, a considerable amount of work needs to be done for its optimization.

3.2 Dip coating

Dip coating is a conventional method of dying to provide quick and easy deposition of materials over a large area [174]. In the case of SCs, deposition via dip coating is a suitable technological tool for large-scale production of OSCs. Dip coating enables a single pass and prompt

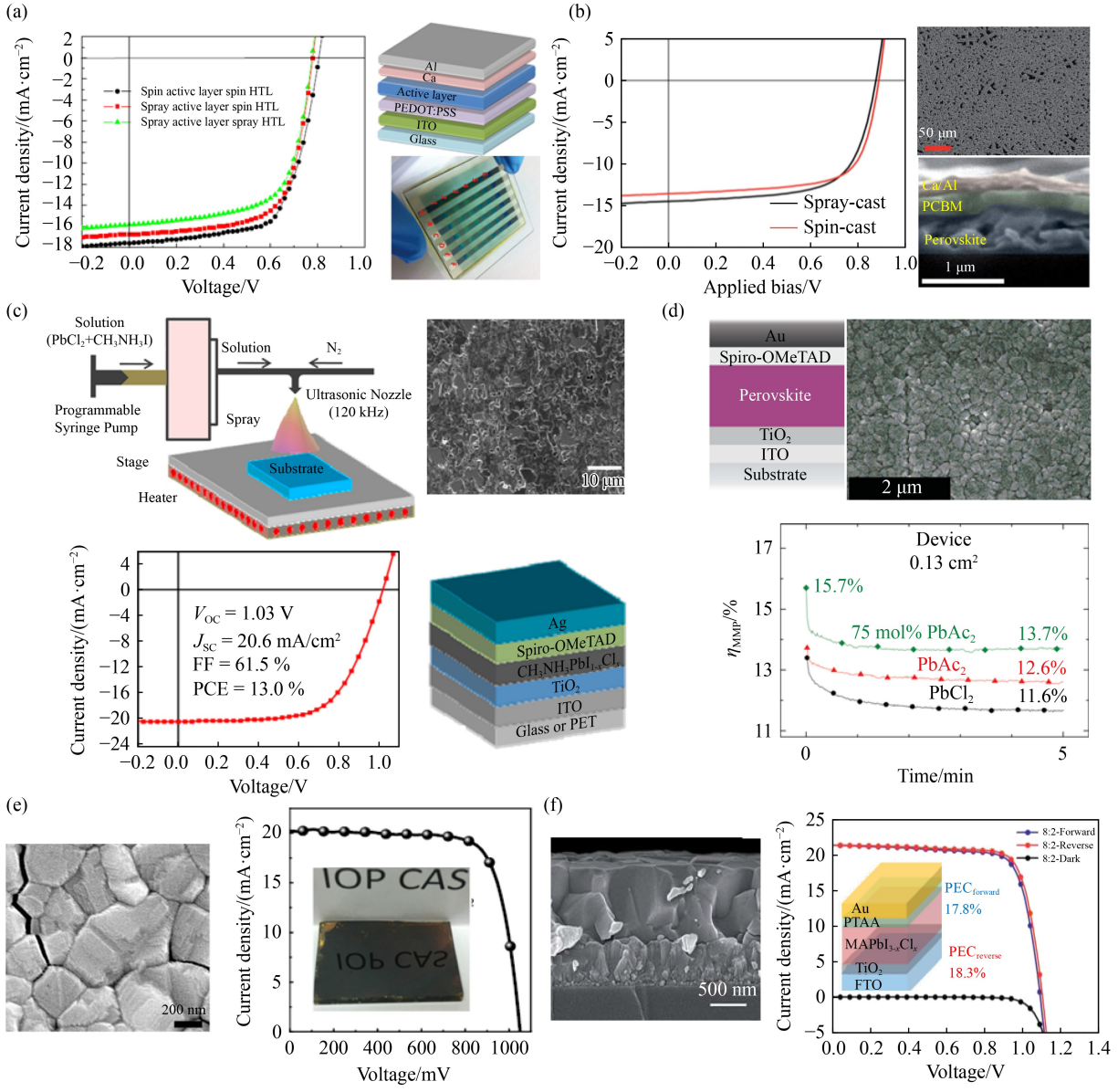

Fig. 11 Photovoltaic performance of SC fabricated by the spray deposition technique.

(a) *J-V* plot of devices, along with the schematic of the device structure and image of arrays of the fabricated device (reprinted with permission from Ref. [166].); (b) *J-V* curves spray deposited $CH_3NH_3PbI_{3-x}Cl_x$ planar SC, along with SEM image of spray-coated $CH_3NH_3PbI_{3-x}Cl_x$ on PEDOT:PSS and cross-sectional SEM image of device (reprinted with permission from Ref. [167]); (c) Schematic illustrating ultrasonic spray-coating process along with SEM images perovskite films on TiO_2/ITO/glass substrates and *J-V* plot of a fabricated PSC with device architecture in the inset (reprinted with permission from Ref. [168]); (d) schematic of implemented device architecture. SEM images of spray deposited perovskite films. Efficiency versus time plot of ITO/TiO_2/$CH_3NH_3Pb_3I_3$/spiro-OMeTAD/Au SCs (reprinted with permission from Ref. [169]); (e) *J-V* plot of the spray deposited PSC, along with photographs and SEM of the spray deposited $CH_3NH_3PbI_3$ films (reprinted with permission from Ref. [170]); (f) cross-sectional SEM image of $MAPbI_{3-x}Cl_x$/TiO_2/FTO film deposited by spraying coating; *J-V* characteristic of $MAPbI_{3-x}Cl_x$ mixed halide PSC (reprinted with permission from Ref. [171]).

formation of thin films with free pin holes [175,176]. In addition, dip-coated films undergo slow natural drying to enable the development of active layer morphology with desired film properties. The fabrication of SCs, especially by dip coating, provides a simple, reliable, and reproducible method particularly designated for thin films, whereby a wet liquid film is deposited on the substrate by immersion. However, the production of the dip-coated film suffers from the disadvantage of slow drying and hence renders incompatible results for high-scale production [177]. The disadvantage of the dip-coating process is that it is slow and can block the screen, hereby creating a major impact on the final product. Dip coating strategically induces the growth of thin films while undergoing an appropriate set of programmed parameters. Additionally, dip coating enables the facilitation of self-assembly of well patterned thin films over a large area coverage with nanoscale control and

optimizations [178]. The controlled optimization allows easy integration on a large scale, thereby benefitting device fabrication. The thin films produced via dip-coating exhibit the least viscous stress toward organic molecules compared to spin coating. The spin-coated film possesses irregular edge effects, formation of cracks, and shrinkage [179]. In photovoltaic, the polymers-based SCs were reported following the dip-coating approach to achieve high performance. An SC composed of poly (3-hexythiophene) and [6,6]-phenyl-C61-butyric methyl with optimized active layers was fabricated. The dip-coated polymer cells displayed a PCE of 3.93% with an FF of 0.63, a J_{sc} of 10.62 mA/cm^2, and a V_{oc} of 0.60 V. The SCs were synthesized in the air without incorporating any annealing treatment [174]. In another study, SCs incorporating ZnO-coated TiO_2 as working electrodes in DSSC were fabricated by the dip-coating method and displayed a high performance. The electrode fabrication followed two working procedures, first spin coating of TiO_2 colloid on FTO glass with consecutive treatment of $TiCl_4$ and second simple dip coating of ZnO on TiO_2 coated FTO electrodes. The electrodes fabricated via the dip coating method also involved utilization of the TiO_2 film in zinc acetate dehydrate and ethanol solution followed by electrode immersion in solution containing N-719 (ruthenium dye) at a working temperature of 70°C. The photovoltaic performance of the SC fabricated by dip coating reveals a clear dominance with a power conversion efficiency of 6.62% in comparison to spin-coated electrodes with an efficiency of 5.45% [180]. Adnan and Lee [181] used a successive dip-coating method for the synthesis of ZnO-covered mesoporous TiO_2 electrodes from a non-halide lead precursor and subsequently used an aqueous system for the formation of thin perovskite films (see Fig. 12). The presence of ZnO induces interfacial layer interactions and causes significant enhancement in adsorption capacity. The successive solid-state ion exchange reaction (SSIER) was optimized to improve the surface morphology, crystallinity, and surface coverage. The fabricated SC demonstrated a PCE of 12.4% with a cost-efficient fabrication approach. The same group reported planar heterojunction PSCs with $MAPbI_3$ perovskite films using the successive dip-coating method. The devices fabricated with the configuration of FTO/c-TiO_2/ZnO/$(CH_3NH_3)PbI_3$/spiro-OMeTAD/MoO_3/Ag showed an efficiency of 12.41%

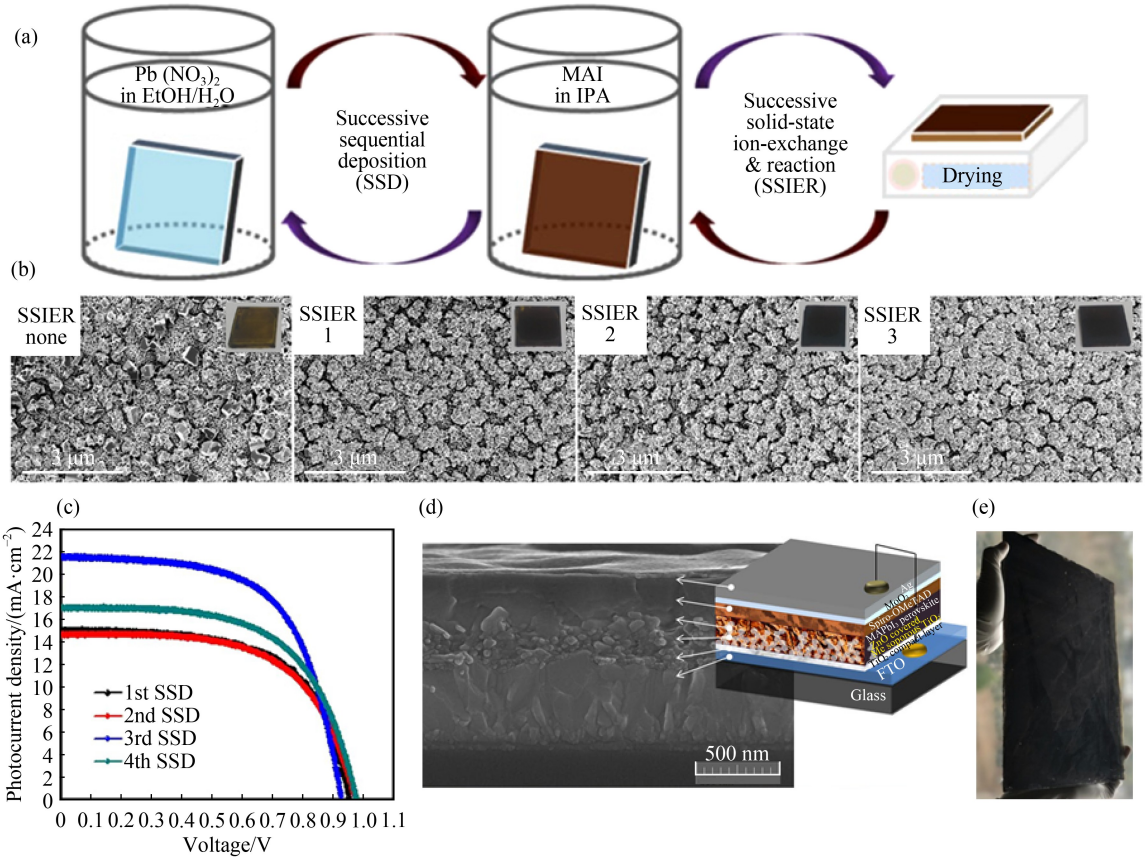

Fig. 12 Photovoltaic performance of dip coating based SC.

(a) Schematic description synthesis of perovskite films using the successive sequential and designated number of SSIER repetitions; (b) SEM images of synthesized $MAPbI_3$ films by SSD and SSIER repetitions along with sample photographs in the inset; (c) *J-V* curves characteristic of device prepared by a mentioned number of SSD cycles followed by 3 SSIER repetitions; (d, e) cross-sectional SEM image of device synthesized by 3 SSDs and 3 SSIER cycles and photograph of perovskite film synthesized on the glass substrate of 780 cm^2, respectively (reprinted with permission from Ref. [181]).

[182]. Recently, the group reported the sequential all dip-coating deposition of $(CH_3)_3NPbI_{3-x}Cl_x$ perovskite materials in the aqueous non-halide lead precursor solution, followed by dip coating in a $(CH_3)_3NI$ and $(CH_3)_3NCl$. The fabricated devices exhibited a high stability and a high photovoltaic performance with a notable efficiency of 15.3% [183].

3.3 Spin coating

The spin coating technique is commonly used to fabricate uniform thin films with a thickness in the range of micrometer to the nanometer. The depositing substrate is mounted on a rotating chuck that rotates the substrate under the action of centrifugal force and surface tension, thereby driving the liquid radially outwards. The combined effect of viscous force and surface tension enables flat deposition on the surface. The thin film formation is ensured through evaporation. The spin coating consists of stages like liquid dispensing, spin up, stable fluid outflow, spin-off and evaporation (drying) [184]. The SC deposition via spin coating allows high thickness and quality assurance of the film based on speed and time optimizations along with ink formulation [185]. The spin coating technique also ensures high reproducibility and uniformity. However, one of the main drawbacks of spin coating is the substrate size. When the substrate size is large, high-speed spinning becomes difficult, and so does film thinning. The efficiency of the spin coating material is very low, and generally,

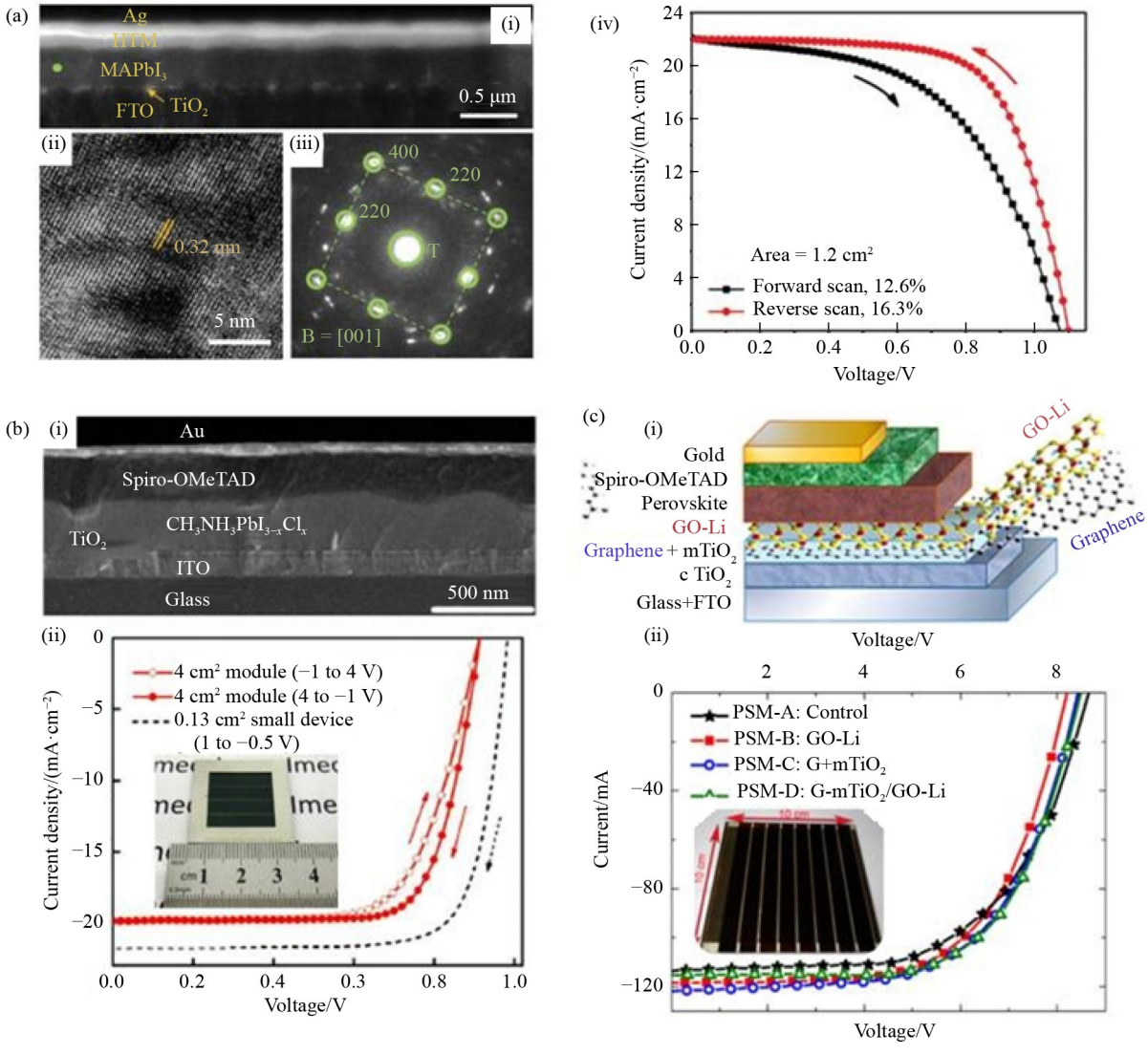

Fig. 13 Photovoltaic performance of spin-coating based SCs and modules.

(a) (i) Cross-sectional TEM image of the fabricated PSC; (ii) high-resolution TEM image of $CH_3NH_3PbI_3$ film; (iii) SAED image of the green spot section pointed out in (a.i); (iv) *J-V* curve for champion SC with 1.2 cm^2 active area (reprinted with permission from Ref. [189]); (b) (i) cross-section SEM image of the device; (ii) *J-V* plot of the 4 cm^2 PSC (inset shows the photograph of 4 cm^2 aperture PSC having 4 sub-cells) (reprinted with permission from Ref. [190]); (c) (i) device architecture PSC; (ii) *J-V* curve of tested modules (inset shows the photograph of the PSC module with an active area of 50 cm^2) (reprinted with permission from Ref. [191]).

95%–98% of the material is disposed of during the spinning process, and only 2%–5% of the material is spread onto the substrate. The efficiency values of ~22.1% were achieved in SCs fabricated via spin coating with an active area of ~0.1 cm^2 [186]. The SC fabrication by spin coating with dimensions greater than 1 cm^2 or larger cells yields a gauging performance to limit their photovoltaic parameters. For instance, enhancing the SC area from 0.1 to 1 cm^2 leads to a 10%–15% drop in the efficiency of SC [187]. Recently Cui et al. [188] incorporated a fine modification in flexible side chains of non-fullerene electron acceptor sand fabricated single-junction OSCs. The cells employing the BTP-4Cl-12 and polymer donor PBDB-TF yield an efficiency of 17%. Yang et al. [189] apprehended $CH_3NH_3PbI_3$ based SCs with an efficiency of 16.3% for an active area of 1.2 cm^2 (see Fig. 13(a)). In addition, Qiu et al. [190] reported a PSC module with an aperture area of 4 cm^2. They spin-coated pinhole-free absorber films with a precursor combination of CH_3NH_3I, $PbCl_2$ and $Pb(CH_3CO_2)_2.3H_2O$. The module exhibited an aperture area PCE of 13.6% and 12.6% after 5 min of maximum power point tracking (see Fig. 13(b)). In another study, Agresti et al. [191] demonstrated an efficiency of 12.6% for large area PSC modules, assembled on a 10 cm × 10 cm substrate area, with eight cells having an active area of 6.32 cm^2 each (see Fig. 13(c)). The study paves the way for the industrial exploitation of graphene/perovskite SCs.

3.4 Slot-die

Slot-die coating is well suited for the deposition of organic, perovskite, and other layers in the device stack. As a pre-metered coating method, it is highly efficient in terms of materials used. It results in very low wastage levels of inks compared to other deposition methods such as spin coating, spray, and screen printing. A coating head is positioned close to and across a substrate or web for a typical slot-die coating process. Ink is then pumped into the head, using a syringe pump, with the ink forced out of a narrow slit along the length of the coating head [192]. The ink forms a liquid bridge between the coating head and the substrate. Thereby, when the substrate is moved past the head, the deposition of a wet film is achieved. Over a given coating width, the thickness of the dry film deposited is controlled by adjusting the flow of ink to the coating head and the speed at which the substrate moves past the head. This allows very fine control of the dry film thickness to within a few nm, as well as the ability to deposit very thin dry films, of tens of nm, up to much thicker films of tens of microns simply by adjusting the ink flow rate or substrate speed. Slot-die coating stands out with a unique blend of enclosed reservoir for coating solution, high degree of film thickness control, low material waste, and ease of integration in roll to roll (R2R) manufacturing for scalable production. In the slot-die method, the thin film coating properties depend on the thickness and stability of wet film [193]. Slot-die coating has several limitations, such as the low-flow limit which causes the break-up of the downstream meniscus and discontinuous formation of films [194,195], the defects related to discontinuous film formation such as rivulets, where the coating breaks into several smaller stripes having gaps, the defects related to air-entrainment which are associated with the upstream meniscus breakup that lead to ‘bubbles’ within the wet film and area around the uncoated substrate, and the dripping or flooding where the ink flow to the head is higher than the coating speed. This leads to the gradual accumulation of the ink at the coating head and the loss of control over film thickness [195]. The slot-die fabrication approach was widely applied and explored for photovoltaic cells based on organic materials due to the non-viscous and low boiling points of the material. Moreover, organic materials exhibit the least changes in composition during solvent evaporation. Specifically, slot-die coating was deployed for deposition of perovskite using single or two-step coated layers [196–198]. The morphology of PSCs coated via the slot-die method varied in the single-step coating procedure. However, air and vacuum quenching yielded a promising and better morphology of the deposited films when procured using dimethylformamide [199]. Lee et al. [199] employed mixed lead precursors consisting of $PbAc_2$ and $PbCl_2$ to fabricate PSC via slot-die coating. The device exhibited an improved photovoltaic performance with an efficiency of 13.3%, a large-area module with an active area of 10 cm^2, and an efficiency of 8.3% (see Fig. 14(a)). Heo et al. [200] reported organic cation additives in lead iodide solutions as a practical approach for the R2R production of PSCs. The sequential deposition was performed in air with the slot-die technique to fabricate SC on glass that exhibited an efficiency of 14.4%. On the other hand, the SC synthesized on the flexible substrate via the R2R method in air displayed an efficiency of 11.0% (see Fig. 14(b)). In another study, the slot-die coating process for manufacturing of PSC and modules was successfully demonstrated with an efficiency of 16.8% and 11.2% (12.5 cm × 13.5 cm), respectively (see Fig. 14(c)) [197]. Recently, Kim et al. [201] reported a two-step slot-die protocol for the preparation of a high-quality perovskite film. A mediator extraction treatment was adopted to convert pre-deposited PbI_2-DMSO complex film into the peculiar porous PbI_2 film with unusual crystallographic orientation. The mediator exchange process in $CH_3NH_3PbI_3$ based SC resulted in an efficiency of 18.3% using slot-die coating on a 10 cm × 10 cm substrate (see Fig. 14(d)). Dou et al. [202] fabricated all blade coated metal halide perovskite cells with an efficiency of 19.6%. However, slot-die coated and partially R2R slot-die coated flexible glass-based cells showed an efficiency of 17.3% and 14.1%, respectively. The developed printing method can be applied to diverse perovskite compositions, enabling a variety of bandgaps to pave the way for the future R2R printing of highly efficient perovskite-perovskite tandem cells. Table 2 lists the

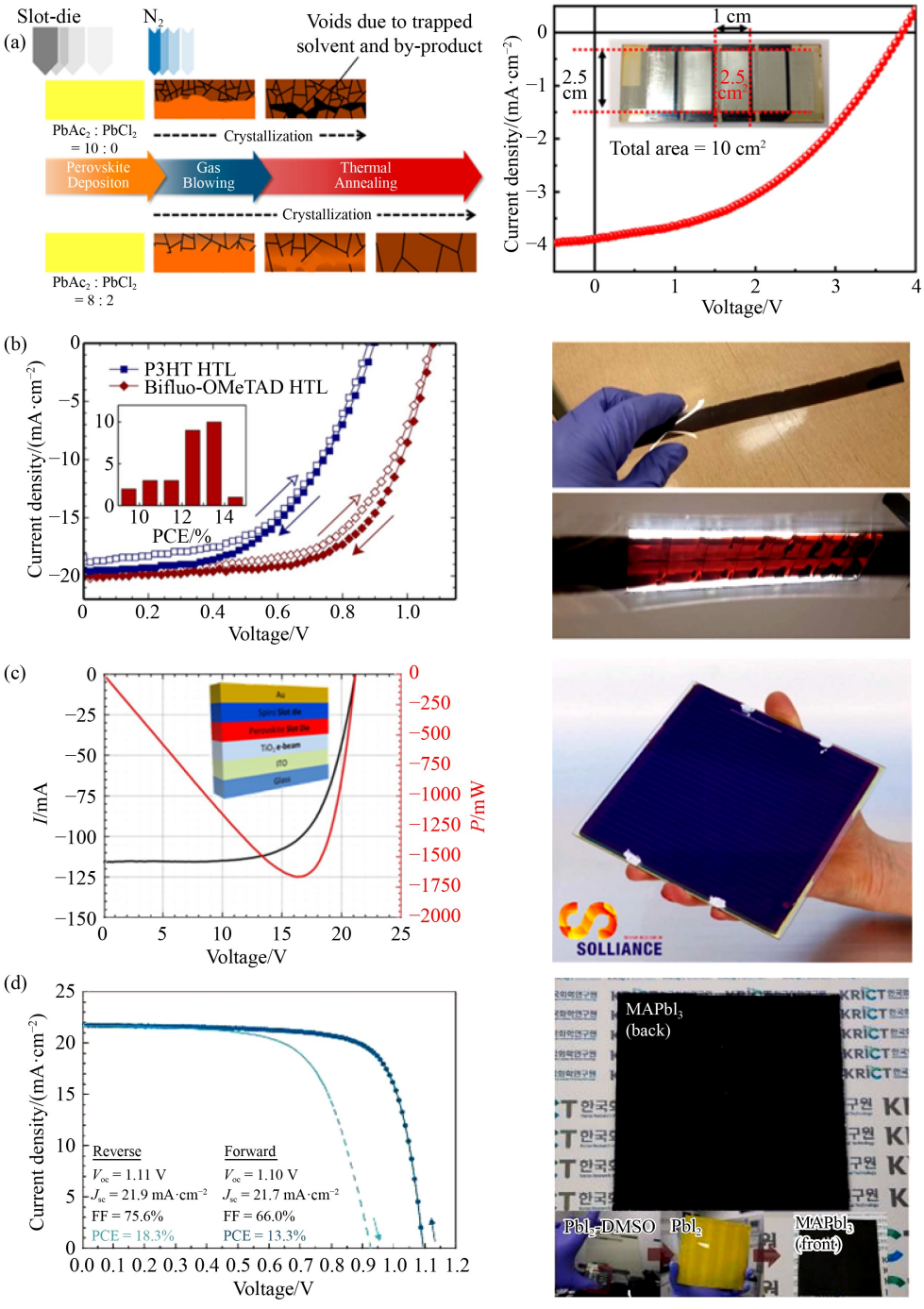

Fig. 14 Photovoltaic performance of slot-die coating-based SCs modules.

(a) Schematic illustrating slot-die mechanism of the perovskite film (left) and *J-V* plot of the synthesized module (right) (reprinted with permission from Ref. [199]); (b) *J-V* plot of SC with device architecture having P3HT and Bifluo-OMeTAD as HTL layer (left) (inset represents PCE of Bifluo-OMeTAD based SC.); R2R slot-die coated perovskite layer (right) (reprinted with permission from Ref. [200]); (c) *I-V* characteristic and power curve of the 6 in. × 6 in. module, with 168.75 cm^2 actual dimension having 25 cells and the inset showing the schematic of device structure (left); photograph of 6 in. × 6 in. fabricated perovskite module (right) (reprinted with permission from Ref. [197]); (d) *J-V* curves of the best performance SC prepared by slot-die method (left); photograph of 10 cm × 10 cm perovskite layer, along with PbI_2-DMSO, PbI_2, and $CH_3NH_3PbI_3$ films (right) (reprinted with permission from Ref. [201]).

photovoltaic parameters of high-performance SCs fabricated by scalable wet synthesis methods.

4 Methods to increase light harvesting in solar cell

4.1 Surface texturing and nanostructured anti-reflection coatings

Changes in the design or structure of SCs are very crucial in order to ensure a maximum light absorption with a significant carrier extraction ability. Researchers have conducted numerous studies on light absorption, carrier collection, electrode design, and structure design, which will help to improve the design of the SCs [204]. It is known that the incident light is not completely absorbed; thus, several device structures have been introduced with light trapping patterns. These patterns increase the generation rate of the photocarrier, which in turn helps to enhance the J_{sc} of an SC. Due to the increased use of light trapping patterns, thinner cells are used for controlling the light because it has a beneficial effect on the V_{oc}. It is observed that the light with a comparatively small angle of incidence gets dispersed in SCs consisting of a light-trapping design. Currently, Si SCs are equipped with random texture structures, but these structures treat the light of all wavelengths in a similar manner and are not capable of controlling the propagation behavior of light. Moreover, random textures do not concentrate on the weak absorption band of SCs, mostly those being near the infrared region. Many researchers are developing light trapping materials and designs to productively utilize incident light. Usually, a quarter wavelength thick anti-reflecting coating (ARC) with real index value which is calculated as the geometric mean of the substrate and air indices, is added to reduce the reflection [205]. Thin transparent films of silicon nitride or silicon dioxide with real index equal to 2 or 1.5, respectively, are used as ARCs in c-Si cells. However, these ARCs give good results only for a certain set of wavelengths and angles of incidence in which the back-reflected wave is reduced due to destructive interference. Other methods such as deposition of several layers with a graded-index can be used to minimize the light reflection. Though this method is considered better for the reduction of light reflection, on the other hand, its processing may be very complicated and costly [206]. To get rid of these issues, a packed array of semiconductor nanostructures is used as a substitute to ARCs, as they provide many advantages: first, they are thin, and secondly, they work effectively for a wide wavelength and angular range. Adiabatic or graded refractive indexes that differ as the area increases (area ~1 m^2) are easily being developed due to the advancement in nanofabrication methods. Production of random designs through wet-chemical etching [207], synthesis of ordered arrays of biomimetic Si nanotips [208], nanocones, domes [209,210], nanowires [211], and

Table 2 Photovoltaic performance of SCs fabricated by scalable wet synthesis methods

Material	J_{sc}/(mA·cm^{-2})	V_{oc}/V	FF/%	Efficiency/%	Ref.
Spray active layer and HTL	15.83	0.78	65.28	8.06	[166]
Spray deposited $CH_3NH_3PbI_{3-x}Cl_x$ planar SC	16.8	0.92	72	11.1	[167]
Spray deposited $CH_3NH_3PbI_{3-x}Cl_x$SC	20.6	1.03	61.5	12	[168]
Spray coating of $CH_3NH_3PbI_3$ SC	22.5	0.95	73	15.7	[169]
Spray coating of $CH_3NH_3PbI_3$ SC	20.27	1.04	75.5	16.03	[170]
Spray deposited $MAPbI_{3-x}Cl_x$ planar hybrid SC (reverse scan)	21.4	1.10	77.6	18.3	[171]
Complete spray deposited SC	16.7	0.87	70	9.9	[172]
Complete spray deposited SC	19.5	0.85	67	9.2	[173]
Dip coating $(CH_3NH_3)PbI_3$	21.53	0.93	62	12.4	[181]
Dip coating $(CH_3NH_3)PbI_3$	20.33	0.95	63	12.41	[182]
Dip coating $(CH_3)_3NPbI_{3-x}Cl_x$	21.31	1.04	69	15.29	[183]
Spin coating PBDB-TF:BTP-4Cl-12	25.6	0.85	77.6	17	[188]
Spin coating $(CH_3NH_3)PbI_3$	21.9	1.10	67.1	16.3	[189]
Spin coating $(CH_3NH_3)PbI_{3-x}Cl_x$	19.9	0.91	75	13.6	[203]
Slot-die $(CH_3NH_3)PbI_3$	19.9	0.89	74	13.3	[199]
Slot-die $(CH_3NH_3)PbI_3$	21.3	1.8	62.3	14.4	[200]
Slot-die $(CH_3NH_3)PbI_3$	22.1	1.03	74	16.8	[197]
Slot-die $(CH_3NH_3)PbI_3$	22	1.12	76.3	18.8	[201]
Slot-die $(CH_3NH_3)PbI_3$	22.4	1.11	69.7	17.31	[202]

dual-diameter nanopillars [212] are a few of the texturing methods used in SCs fabrication. An array of nanocones by nano-sphere lithography patterned into a planar a-Si film is shown in Fig. 15(a) [209]. It is observed that the texture of the surface could reduce the reflection up to ~40% from the planar a-Si surface [209]. Besides, studies on the base diameter, height, and aspect ratio of nanocones were done to realize broadband, omni-directional ARCs [210]. It is observed that at higher values of aspect ratio, structures could be used as better ARCs. Likewise, at lower values of aspect ratio, structures were found to disperse light productively and can easily be integrated for guided resonances of SCs. Moreover, reflection can be reduced with the help of structures that are produced on the front surface. These structures provide a productive way to couple light into a semiconductor layer and thus, resulting in a reduction of light reflection. For instant, to obtain a certain amount of light trapping, transparent conductive oxides (also used as electrical contacts) in several SCs are coarsened.

Dielectric nanoparticles (NPs) with high index values such as TiO_2 are highly capable of redistributing light in the absence of parasitic absorption of metallic back reflectors [213]. A triple-layer coating of TiO_2/SiO_2 structure was proposed by Ye et al. [214] to serve as a broadband abrasion-resistant antireflective film in SC. On the other hand, trapping techniques were introduced by Chen et al. [215], and these techniques were developed from ZnO microspheres and are depicted in Fig. 15(b). A CdS-CdTe p-n junction of nanotube array was proposed by Liyanage and Nath [216]. A 50% boost in the light conversion efficiency was noticed, as shown in Fig. 15(c). Moreover, for a light absorption layer of 10% or even lesser, it was capable of producing the exact photocurrent as the bulk film. The range of the solar absorption can be increased, and an effective charge separation can be obtained with the help of ternary [ZnS-CdS-$Cu_{2-x}S$] hetero-nanorods developed by Zhuang et al. [217] (see Fig. 15(d)). An increase of 5% in J_{sc} and a 17.1% enhancement in the PCE was recorded when an ARC based on randomly distributed micro-scale pyramids was introduced on the glass side of an inverted p-i-n

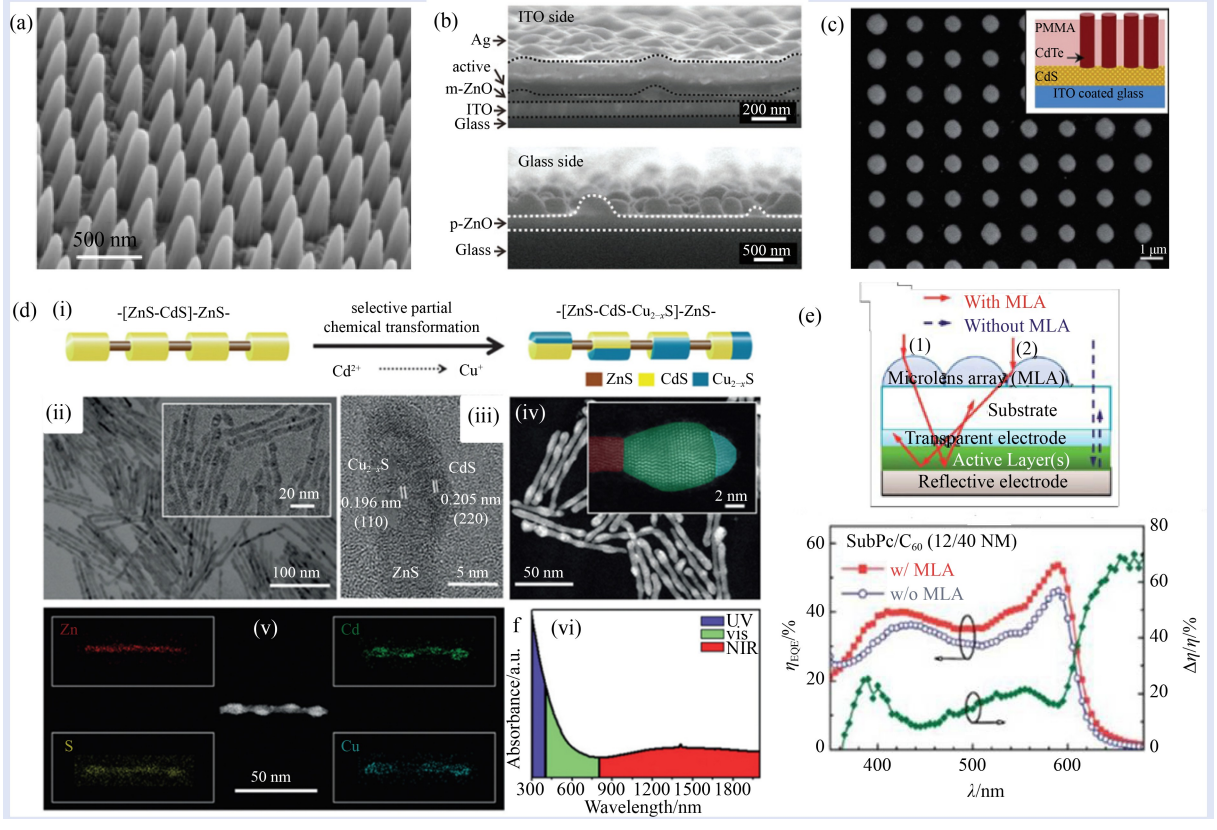

Fig. 15 Various surface engineering methods in SCs.

(a) SEM of nanocones array on a-Si SC (reprinted with permission from Ref. [209]); (b) SEM image of ZnO microsphere (reprinted with permission from Ref. [215]); (c) SEM image of CdTe nanotubes deposited on CdS layer (left) (inset shows the schematic of deposited layers) (reprinted with permission from Ref. [216]); (d) (i) schematic showing the synthesis of ternary ZnS-CdS-$Cu_{2-x}S$; (ii−v) TEM, HRTEM, HAADF-STEM image and EDS of ZnS-CdS-$Cu_{2-x}S$, respectively; (vi) absorption curve of ZnS-CdS-$Cu_{2-x}S$ (reprinted with permission from Ref. [217]); (e) schematic representing light interaction with OSC in the presence and absence of microlens array, along with EQE spectra of the fabricated device (reprinted with permission from Ref. [219]).

PSCs [218]. The anti-reflecting coating in OSCs is mostly based on a microlens array. For instance, a light-trapping arrangement in concurrence with an aligned micro-apertures array is shown in Fig. 15(e) [219]. It is found that the angular and polarization distributions of the scattered light need to be controlled when the shape and size of the nanostructure are altered. Considering this, several nanostructures in different morphological dimensions were studied to improve light trapping [220–222]. Altering the parameters of these nanostructures is expected to improve the PCE of the SC. A light-trapping structure and a composite functional coating with a low reflectivity, a high conductivity, and a high absorption can help in efficient light harvesting.

4.2 Plasmonic assisted light harvesting

Light absorption can be increased with the help of structures exhibiting plasmonic properties. This can be done by trapping the free-propagating plane waves via NPs, or it can be done when the plasmon polaritons at the surface propagate all over the interface or when it acts as a coupling semiconductor for the near-field sub-wavelength antenna Plasmon [223,224]. Periodic metal nanostructures suited at the top surface of SCs assist in the dispersion and guiding of light via phenomena like localized surface plasmon and surface plasmon polariton [225]. The overall interaction creates a longer optical path and thus, results in an improved light absorption. Using the concept of periodic plasmonic layer, Pala et al. [225] demonstrated an increase in the efficiency of the SC. This was achieved by integrating an SC structure made of a thin layer of Si and combining it with Ag nanostrips of ~50 nm at the front surface of the cell. In another study, Lee et al. [226] reported the improvement of trapping light from the guided-mode resonance in SCs. Two-filling factor asymmetric binary grating was used for this study, and it was found that about 40% of efficiency can be improved in comparison with a planar Si thin film. Chao et al. [227] used the finite difference time domain method and observed an increase in light trapping when a plasmonic amorphous Si photovoltaic cell is used. On the other hand, Rockstuhl et al. [228] investigated the techniques which were based on the optimal design of 1D and 2D plasmonic SCs. Moreover, the efficiency of the SC can be enhanced by texturing the back surface. Bai et al. [229] conducted simulations to study the correlation between the structure of the Si SC and the absorption efficiency. They pointed out that an increase of about 12.5% in efficiency is achieved at certain optimized parameters. For amorphous Si SC, Ferry et al. [230] investigated nano-imprinted hole patterns covered with plasmonic Ag structures and served as back reflectors. Sai et al. [231] used a honeycomb-like Al pattern to deposit the Ag layer and incorporated it as a back reflector to realize μc-Si based SC. The patterned back reflector improved the external quantum efficiency by 23%, i.e., from 16.8% to 20.7%. Likewise, the two-dimensional plasmonic grating was applied on the back surface of the Si SC by Mokkapati et al. [232], and it was concluded that there is the possibility of ideal design parameters. Mendes et al. [233] studied a new type of plasmonic light trapping back reflector, consisting of colloidal metal particles produced via solution techniques. An improvement in J_{sc} and absorption is observed since the metal particles distribute themselves uniformly at the Si surface. Many researchers did not limit their study to plasmonic structures applied at the front and back surface of the cells; instead, they also investigated the effect of plasmonic NPs in the layers of the SC. Controlling several parameters of the metal particles, such as the composition and morphological dimensions etc., can help regulate the light absorption efficiency in the visible-near-infrared region. Metal NPs have a remarkable effect on plasmon resonance due to the recent design of SCs [204]. Nakayama et al. [234] examined the Ag NPs of numerous dimensions and studied the effect of the non-uniform distribution of NPs on the surface of the single-junction GaAs SC. Skrabalak et al. [235] explained that the physical procedure of the surface plasmon resonance effect of metal nanostructures increased the photoabsorption of SCs (see Fig. 16(a)). Among all the nano-crystals, it is found that Au nano-crystals have significant advantages in light absorption as they easily mix with semiconductors and a steady composite coupling structure is formed. Lee et al. [236] incorporated Au NPs in the transport layer and reported an enhanced light absorption. On the other hand, Yuan et al. [237] added Au NPs in the dense layer of a thin-film SC, which had a planar heterojunction structure. It was concluded that the electrons got excited by hot electron injection, which remarkably increased the efficiency of SCs. The relationship between the size and charge separation of Au NPs via photovoltaic conversion was investigated by Reineck et al. [238]. They concluded that both the parameters were inversely proportional to each other; in other words, the charge separation process would become significantly effective when the size of the Au particle is decreased. Moreover, the internal quantum productivity reached 13.3% when very small Au particles of approximately 5 nm were used. Schaadt et al. [239] described the significance of the relationship between the dimensions of the metal NPs and the efficiency of SCs. Processes influencing the transfer of energy like illumination conditions, the structure of the device and morphologies etc. was studied by Xu et al. [240]. This study concluded that the energy transfers in different arrangements of plasmonic metallic semiconductors in combination with dielectric layers. TiO_2-Al_2O_3-Au electrode was found to be the best of all the composite structures of TiO_2 nanotubes and exhibited a better response to light not only in the UV region but also in the

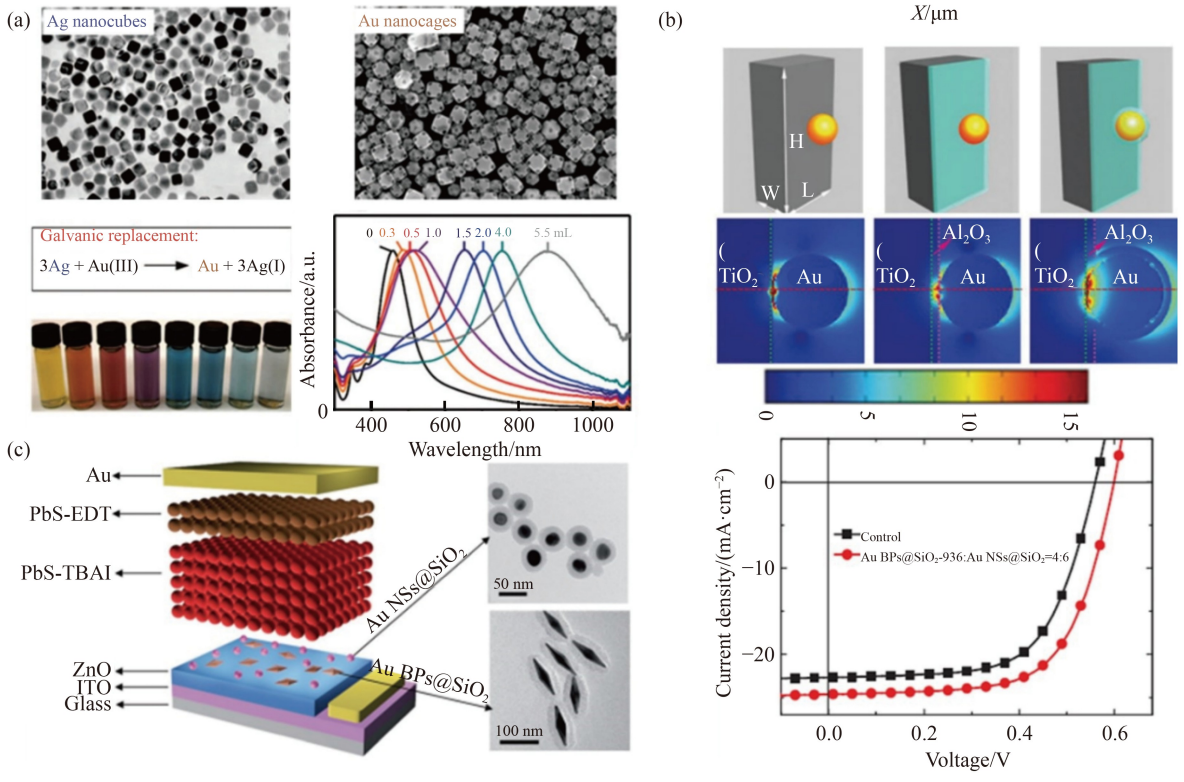

Fig. 16 Various strategies for light harvesting in SCs.

(a) TEM image and the resultant surface plasmon resonance plot of Au nanorods with varying concentrations of Ag^+ (reprinted with permission from Ref. [235]); (b) schematic diagram of TiO_2 nanotube-Au, TiO_2 nanotube-Al_2O_3-Au and TiO_2 nanotube-Au-Al_2O_3 (along with electric field spatial distribution in the *y*-plane under 570 nm incident light irradiation (reprinted with permission from Ref. [240]); (c) schematic of PbS SC, TEM images of Au nanospheres@SiO_2 and Au bipyramids@SiO_2 (*J*-*V* plot of SC with/without the mixture of Au nanospheres@SiO_2 and Au bipyramids@SiO_2) (reprinted with permission from Ref. [241]).

visible regions (Fig. 16(b)). Ma et al. [241] incorporated di-pyramidal Au NPs and Au spheres and reported an increase of 9.58% in the PCE of the SC with device architecture ITO/ZnO/PbS-TBAI/PbS-EDT/Au (Fig. 16(c)). Moreover, in the recent generation of photovoltaic, studies were mainly based on plasmonic materials incorporated polymeric SCs [242]. The productivity of the photoelectric conversion and the light harvesting is highly improved with the use of plasmonic materials. Furthermore, plasmonic materials evenly assist in the absorption of light and carrier transport, resulting in the development of cheap and high efficiency full spectrum SCs.

4.3 Mechanical methods

4.3.1 Sun tracker systems

The solar tracking or the sun-tracking systems are an important part of solar power plants to maximize the absorption of solar light, thereby adjusting the panel automatically to ensure maximum exposure of the panel toward sun rays at 90°. The component to ensure this is by utilizing photo-sensors, thereby measuring the solar radiance and providing feedback signals based on the current stature of the panel deployed. The automatic positioning of the solar panel toward the direction of sun rays is calculated based on the current position of the sun and the seasonal movement. The panels are oriented using two linear actuators. The first one controls seasonal orientation or azimuth adjustment, while the second optimizes day or zenith adjustments [243]. The sun-tracking systems are divided into the controlling unit and the hardware. The controlling unit optimizes the panel in the form of programmed language while the hardware consists of the mounting set up, solar panel, and the micro-controller. The design of the sun tracker should be considered before its mounting and applicability to ensure durability and enhance mobility. The presence of a solar tracker can greatly enhance the performance of solar panels. The alignment of the solar tracker boosts the energy gain on photovoltaic arrays. The solar trackers must exhibit the following important characteristics [244]: parallel console type or single-column structure, single or binary moving motor setup, presence of light-sensing setup, auxiliary or automatic energy supply, moving setup in accordance to light calendar, sequential or continuous movement, and qutomatic orientation

adjustment.

Sun tracking systems are mainly classified as mechanical or passive trackers and electrical or active trackers. The mechanical trackers are generally based on thermal expansion of matter (Freon) or shape memory effect on alloys. The mechanical tracker is comprised of a few actuators operating against each other and being balanced by equal illumination. The differential illumination of the actuators results in the unbalancing of forces between them and hence is used to control the orientation of the setup toward a direction of balanced illumination. The mechanical tracking systems are the least complex. However, they are functional at a low efficiency with the limitation of being nonfunctional at low temperatures. Passive trackers, despite being cost-efficient, are not widely used [245]. Electrical or active trackers are categorized as a microprocessor or electro-optical sensor-based, computer-controlled time and data-based, auxiliary bifacial based or a combination of all three systems. The electro-optical sensor-based setup comprises of a pair of photo-resistors or photovoltaic SCs connected in an anti-parallel way to attain equal illumination, which is electrically balanced to permit the control on the driving motor. In a bifacial setup, SCs perform sensing and controlling of the system toward desired positions and finally, in the third setup, a computer measures the sun position with respect to time and date and controls the system with algorithms by the creation of desired signals [246].

4.3.2 Reflective systems

Reflective systems are also used in tracking solar energy via solar energy collectors. The reflective system continuously monitors the positioning of the sun across the sky in order to ensure their maximum reflection toward the collector. The setup comprises a major reflector mounted onto a movable platform to ensure movement in all directions. The movement of the reflective system is controlled via the reflection of light from the reflector toward a position detecting target through a minor reflector. When reflection takes place toward a neutral position on the target, the major reflector in the setup is positioned toward direct light from where the energy is diverted toward the collector. In case of reflection from the points other than the neutral position, the major reflector is adjusted in one or both directions until incident rays are normal to its surface before their diversion toward the collector. Reflective systems form a vital part toward the consideration of solar light in solar thermal power plants. The reflectors must exhibit a good stability, a high reflectivity, a low parasitic absorption, and an excellent durability. The purpose of using reflective systems is to couple large amount of incident energy onto the layers of SCs [247]. The reflectors mainly contain second surface silvered glass with glass substrate coated with reflective layers of silver guarded by a layer of copper and coatings of several protective paints [248,249]. The protective layer in recent years containing copper has been replaced by a cationic solution with $Pb(SnCl_2)$ and an anionic solution comprising of hydroxyl ions (with NaOH), forming a water-soluble precipitate on the silver surface to avoid corrosion [250]. Apart from silver reflective systems, a cost-efficient alternative in the form of aluminum reflectors has been explored with a layer of polished aluminum deposited over the substrate along with the protective coatings in order to improve durability. The protective layers for aluminum-based reflectors are composed of SiO_2 layers to ensure protection against corrosion and abrasion [251]. Additionally, silvered polymer-based films have also been procured for reflectors [252]. This reflector is composed of a silver layer deposited on a substrate protected by a polymeric layer. These reflectors are flexible, lightweight exhibiting ease of adhesion toward rigid substrates.

4.3.3 Fresnel lens

A light-concentrating technology is used to maximize the capturing of solar intensity, and Fresnel lens performs the same task. Fresnel lens provides advantages like small volume, lightweight, low cost, mass productivity in addition to an effective increase in energy density. Earlier, Fresnel lenses made of glass were used as collimators in lighthouses [253]. The lenses of glass are an attractive option for use in temperature or glazing. In contrast, poly-methyl methacrylate is an appropriate material for lens-making due to characteristics like lightweight, transparency, and stability at high temperatures. These characteristics make it an ideal choice for Fresnel lens. The quality of Fresnel lens has seen a vast improvement with the developments in modern plastics, novel molding methods, and computer-controlled methods turning machines. These lenses can be molded via pressure or injection molding methods, sliced or extruded from various plastic materials, reducing production costs. Fresnel lenses in solar applications are used as solar concentrators due to their high optical efficiency in addition to their lightweight and cost efficiency [254].

However, Fresnel lenses as energy concentrators have been used since the 1960s. The Fresnel lens for solar energy concentrations is classified as an imaging and non-imaging system. An imaging Fresnel prism consists of a continuous chain of prisms with each prism corresponding to the slope of the lens surface compared to a normal lens. Initially, Fresnel lenses for solar concentration were not designed for solar ray collection despite being used for imaging devices. Such an imaging

Fresnel lens worked on the reflection, and the light was reflected from the ion object to form an image in the focal plane highly influenced by aberrations due to defects in the prism tips and grooves. The photovoltaic generation of electricity setups is often equipped with imaging type Fresnel lenses with precise tracking by monitoring the lens focus on the receiver [255]. The imaging Fresnel lenses are used in photovoltaic applications, solar lighting, and solar pumped laser. Fresnel lenses are more widely used in solar applications for non-imaging systems due to the non-demanding nature of imaging quality in photovoltaic cells. Instead, SCs require design flexibility with uniform flux concentrators capable of adjusting solar disk size, solar spectrum, and reduction in tracking errors. Hence, Fresnel lenses dedicated for non-imaging solar tracking are generally convex in shape to yield a high concentration ratio and flux distribution while exhibiting short focal length. The non-imaging Fresnel lenses work on the effect of chromatic abrasions.

5 Future perspectives

Despite the substantial developments in recent years, additional advancement is required for photovoltaic to gain commercial success. Hence, it is essential to discover and invent materials comprising direct bandgaps and enhanced optoelectronic properties. Furthermore, the exciton effect and electron-phonon coupling result in unwanted electron-hole recombination hampering carrier transport. These inherent electronic properties require proper attention, and forthcoming research should emphasize manufacturing efficient light-absorbing direct bandgap materials. In the case of PA layers prepared by solution-based methods, many intermediate steps are involved. Thus, there is a need for standardized methodology and processing environments to get a dense, uniform, and pinholes deficit high-quality film. Moreover, the grain boundary should be minimized, as it consists of high defects density states acting as recombination centers and hinders charge transport. Apart from possessing a suitable optical gap and a good structural ability, a PV absorber should have a high defect tolerance without intrinsic deep defect levels. To minimize the charge carrier loss, the interface of the charge transporting materials and PA material has to be optimized by band alignment through the use of rational HTL/ETL in the device architecture. In addition, the defect passivation still remains a major unresolved task in photovoltaic. The defect passivation protocol should provide strength against oxidation, compositional optimization of the PA layer, and reduced interfacial recombination. Moreover, the device structure is vital in formulating high-efficiency SCs. Photovoltaic performance restraining is caused due to the inefficient interaction and interfacial recombination of transport layers and contacts. Consequently, further exploration/optimization of charge transport layers, the interfacial combination effects, and appropriate device structure are needed for the enhancement in photovoltaic efficiency. With the investigation of new synthesis approaches and tailoring of material properties, an improvement can be expected in the performance of SC in the near future. We look forward to high proficiency and environmentally friendly SCs creating a big contribution in the field of photovoltaic.

6 Concluding remarks

Research methods and directions toward high-efficiency stable SCs were presented in this review. Different absorber material and device architecture were covered for achieving enhanced light absorption, electrical properties, stability, and higher PCE in SCs. The strategies in materials and large area deposition coating techniques for achieving high-efficiency SCs were elaborated. For further improvements of photovoltaic performance, a proper coating procedure should be applied to achieve defectless high-quality absorber films. Various light-harvesting strategies like anti-reflecting coatings, surface texturing, patterned nanostructure growth, plasmonics, and mechanical methods are discussed. The review summarized the results achieved in the laboratory and is helpful for production of high-efficiency SCs. Research strategies to further improve the efficiency of SCs and future perspective of this rapidly advancing field are highlighted.

Acknowledgment This work was supported by an NPRP grant from Qatar National Research Fund under the grant number NPRP12S-0131-190030. The statements made herein are solely the responsibility of the authors.

References

1. Rapier R. Fossil fuels still supply 84 percent of world energy—and other eye openers from BP's annual review. 2020, available at the website of forbes.com
2. Shaikh J S, Shaikh N S, Sheikh A D, et al. Perovskite solar cells: in pursuit of efficiency and stability. Materials & Design, 2017, 136: 54–80
3. Becquerel M E. On electrod effect under the influence of solar radiation. Proceedings of the Academy of Science, 1839, 9: 561−567 (in French)
4. Xu T, Yu L. How to design low bandgap polymers for highly efficient organic solar cells. Materials Today, 2014, 17(1): 11–15
5. Shockley W, Queisser H J. Detailed balance limit of efficiency of p-n junction solar cells. Journal of Applied Physics, 1961,

32(3): 510–519
6. Sze S, Ng K K. Physics of Semiconductor Devices. Wiley Online Books, 2006
7. Singh P, Ravindra N M. Temperature dependence of solar cell performance —an analysis. Solar Energy Materials and Solar Cells, 2012, 101: 36–45
8. Qi B, Wang J. Fill factor in organic solar cells. Physical Chemistry Chemical Physics, 2013, 15(23): 8972
9. Guo X, Zhou N, Lou S J, et al. Polymer solar cells with enhanced fill factors. Nature Photonics, 2013, 7(10): 825–833
10. You J, Dou L, Hong Z, et al. Recent trends in polymer tandem solar cells research. Progress in Polymer Science, 2013, 38(12): 1909–1928
11. You J, Chen C, Hong Z, et al. 10.2% power conversion efficiency polymer tandem solar cells consisting of two identical sub-cells. Advanced Materials, 2013, 25(29): 3973–3978
12. Fan X, Guo S, Fang G, et al. An efficient PDPPTPT: PC61BM-based tandem polymer solar cells with a Ca/Ag/MoO_3 intermediate layer. Solar Energy Materials and Solar Cells, 2013, 113: 135–139
13. Zhao D, Tang W, Ke L, et al. Efficient bulk heterojunction solar cells with poly[2, 7-(9, 9-dihexylfluorene)-alt-bithiophene]and 6, 6-phenyl C61 butyric acid methyl ester blends and their application in tandem cells. ACS Applied Materials & Interfaces, 2010, 2(3): 829–837
14. Guo Z, Lee D, Schaller R D, et al. Relationship between interchain interaction, exciton delocalization, and charge separation in low-bandgap copolymer blends. Journal of the American Chemical Society, 2014, 136(28): 10024–10032
15. Kim J, Yun M H, Kim G H, et al. Synthesis of PCDTBT-based fluorinated polymers for high open-circuit voltage in organic photovoltaics: towards an understanding of relationships between polymer energy levels engineering and ideal morphology control. ACS Applied Materials & Interfaces, 2014, 6(10): 7523–7534
16. Chen H Y, Lin S, Sun J Y, et al. Morphologic improvement of the PBDTTT-C and PC71BM blend film with mixed solvent for high-performance inverted polymer solar cells. Nanotechnology, 2013, 24(48): 484009
17. An T K, Kang I, Yun H, et al. Solvent additive to achieve highly ordered nanostructural semicrystalline DPP copolymers: toward a high charge carrier mobility. Advanced Materials, 2013, 25(48): 7003–7009
18. Guan Z, Yu J, Huang J, et al. Power efficiency enhancement of solution-processed small-molecule solar cells based on squaraine via thermal annealing and solvent additive methods. Solar Energy Materials and Solar Cells, 2013, 109: 262–269
19. Tan M J, Zhong S, Li J, et al. Air-stable efficient inverted polymer solar cells using solution-processed nanocrystalline ZnO interfacial layer. ACS Applied Materials & Interfaces, 2013, 5(11): 4696–4701
20. Elumalai N K, Vijila C, Jose R, et al. Simultaneous improvements in power conversion efficiency and operational stability of polymer solar cells by interfacial engineering. Physical Chemistry Chemical Physics, 2013, 15(43): 19057
21. Tan Z, Li S, Wang F, et al. High performance polymer solar cells with as-prepared zirconium acetylacetonate film as cathode buffer layer. Scientific Reports, 2015, 4(1): 4691
22. Lu L, Yu L. Understanding low bandgap polymer PTB7 and optimizing polymer solar cells based on it. Advanced Materials, 2014, 26(26): 4413–4430
23. Wysocki J J, Rappaport P. Effect of temperature on photovoltaic solar energy conversion. Journal of Applied Physics, 1960, 31(3): 571–578
24. Fan J C C. Theoretical temperature dependence of solar cell parameters. Solar Cells, 1986, 17(2−3): 309–315
25. Singh P, Singh S N, Lal M, et al. Temperature dependence of *I–V* characteristics and performance parameters of silicon solar cell. Solar Energy Materials and Solar Cells, 2008, 92(12): 1611–1616
26. Goetzberger A, Hebling C. Photovoltaic materials, past, present, future. Solar Energy Materials and Solar Cells, 2000, 62(1−2): 1–19
27. Hosenuzzaman M, Rahim N A, Selvaraj J, et al. Global prospects, progress, policies, and environmental impact of solar photovoltaic power generation. Renewable & Sustainable Energy Reviews, 2015, 41: 284–297
28. Subtil Lacerda J, van den Bergh J C J M. Diversity in solar photovoltaic energy: implications for innovation and policy. Renewable & Sustainable Energy Reviews, 2016, 54: 331–340
29. Yoshikawa K, Kawasaki H, Yoshida W, et al. Silicon heterojunction solar cell with interdigitated back contacts for a photoconversion efficiency over 26%. Nature Energy, 2017, 2(5): 17032
30. Peng J, Lu L, Yang H. Review on life cycle assessment of energy payback and greenhouse gas emission of solar photovoltaic systems. Renewable & Sustainable Energy Reviews, 2013, 19: 255–274
31. Tyagi V V, Rahim N A A, Rahim N A, et al. Progress in solar PV technology: research and achievement. Renewable & Sustainable Energy Reviews, 2013, 20: 443–461
32. Goetzberger A, Hebling C, Schock H W. Photovoltaic materials, history, status and outlook. Materials Science and Engineering R Reports, 2003, 40(1): 1–46
33. Miles R W, Hynes K M, Forbes I. Photovoltaic solar cells: an overview of state-of-the-art cell development and environmental issues. Progress in Crystal Growth and Characterization of Materials, 2005, 51(1−3): 1–42
34. El Chaar L, lamont L A, El Zein N. Review of photovoltaic technologies. Renewable & Sustainable Energy Reviews, 2011, 15(5): 2165–2175
35. Avrutin V, Izyumskaya N, Morkoç H. Semiconductor solar cells: recent progress in terrestrial applications. Superlattices and Microstructures, 2011, 49(4): 337–364
36. Green M A, Dunlop E D, Hohl-Ebinger J, et al. Solar cell efficiency tables (Version 55). Progress in Photovoltaics: Research and Applications, 2020, 28(1): 3–15
37. Braga A F B, Moreira S P, Zampieri P R, et al. New processes for the production of solar-grade polycrystalline silicon: a review. Solar Energy Materials and Solar Cells, 2008, 92(4): 418–424
38. Bruton T M. General trends about photovoltaics based on

crystalline silicon. Solar Energy Materials and Solar Cells, 2002, 72(1-4): 3–10
39. van der Zwaan B, Rabl A. Prospects for PV: a learning curve analysis. Solar Energy, 2003, 74(1): 19–31
40. Keogh W M, Blakers A W. Accurate measurement, using natural sunlight, of silicon solar cells. Progress in Photovoltaics: Research and Applications, 2004, 12(1): 1–19
41. Hanoka J I. An overview of silicon ribbon growth technology. Solar Energy Materials and Solar Cells, 2001, 65(1−4): 231–237
42. Peng K, Lee S T. Silicon nanowires for photovoltaic solar energy conversion. Advanced Materials, 2011, 23(2): 198–215
43. Gangopadhyay U, Jana S, Das S. State of art of solar photovoltaic technology. Conference Papers in Energy, 2013, 2013: 764132
44. Mundo-Hernández J, de Celis Alonso B, Hernández-Álvarez J, et al. An overview of solar photovoltaic energy in Mexico and Germany. Renewable & Sustainable Energy Reviews, 2014, 31: 639–649
45. Boutchich M, Alvarez J, Diouf D, et al. Amorphous silicon diamond based heterojunctions with high rectification ratio. Journal of Non-Crystalline Solids, 2012, 358(17): 2110–2113
46. Subhan F E, Khan A D, Hilal F E, et al. Efficient broadband light absorption in thin-film a-Si solar cell based on double sided hybrid bi-metallic nanogratings. RSC Advances, 2020, 10(20): 11836–11842
47. Matsui T, Bidiville A, Maejima K, et al. High-efficiency amorphous silicon solar cells: impact of deposition rate on metastability. Applied Physics Letters, 2015, 106(5): 053901
48. Sai H, Matsui T, Kumagai H, et al. Thin-film microcrystalline silicon solar cells: 11.9% efficiency and beyond. Applied Physics Express, 2018, 11(2): 022301
49. Britt J, Ferekides C. Thin-film CdS/CdTe solar cell with 15.8% efficiency. Applied Physics Letters, 1993, 62(22): 2851–2852
50. Cdte C, Solar P, Wu X, et al. 16.5%-efficient CdS/CdTe polycrystalline thin-film solar cell. Renewable Energy, 2001, 22–26
51. Aberle A G. Thin-film solar cells. Thin Solid Films, 2009, 517(17): 4706–4710
52. Powalla M, Bonnet D. Thin-film solar cells based on the polycrystalline compound semiconductors CIS and CdTe. Advances in OptoElectronics, 2007, 2007: 097545
53. Wang D, Yang R, Wu L, et al. Band alignment of CdTe with MoO_x oxide and fabrication of high efficiency CdTe solar cells. Solar Energy, 2018, 162: 637–645
54. Kazmerski L L, White F R, Morgan G K. Thin-film $CuInSe_2$/CdS heterojunction solar cells. Applied Physics Letters, 1976, 29(4): 268–270
55. Mickelsen R A, Chen W S. Development of a 9.4% efficiency thin-film $CulnSe_2$/CdS solar cell. In: Proceeding of Photovoltaic Specialists Conference, Institute of Electronics Engineers, 1981, 800–804
56. Wang Y C, Shieh H P D. Double-graded bandgap in Cu(In, Ga)Se_2 thin film solar cells by low toxicity selenization process. Applied Physics Letters, 2014, 105(7): 073901
57. Cui X, Yun D, Zhong C, et al. A facile route for synthesis of $CuIn_xGa_{1-x}Se_2$ nanocrystals with tunable composition for photovoltaic application. Journal of Sol-Gel Science and Technology, 2015, 76(3): 469–475
58. Reinhard P, Pianezzi F, Bissig B, et al. Cu(In, Ga)Se_2 thin-film solar cells and modules—a boost in efficiency due to potassium. IEEE International Journal of Photovoltaics, 2015, 5(2): 656–663
59. Fischer J, Larsen J K, Guillot J, et al. Composition dependent characterization of copper indium diselenide thin film solar cells synthesized from electrodeposited binary selenide precursor stacks. Solar Energy Materials and Solar Cells, 2014, 126: 88–95
60. Rampino S, Armani N, Bissoli F, et al. 15% efficient Cu(In, Ga)Se_2 solar cells obtained by low-temperature pulsed electron deposition. Applied Physics Letters, 2012, 101(13): 132107
61. Nakada T. Invited Paper: CIGS-based thin film solar cells and modules: unique material properties. Electronic Materials Letters, 2012, 8(2): 179–185
62. Kapur V, Kemmerle R, Bansal A, et al. Manufacturing of 'ink based' CIGS solar cells/modules. In: 2008 33rd IEEE Photovoltaic Specialists Conference, San Diego, CA, USA, 2008
63. Romeo A, Terheggen M, Abou-Ras D, et al. Development of thin-film Cu(In, Ga)Se_2 and CdTe solar cells. Progress in Photovoltaics: Research and Applications, 2004, 12(23): 93–111
64. Ramanathan K, Contreras M A, Perkins C L, et al. Properties of 19.2% efficiency ZnO/CdS/$CuInGaSe_2$ thin-film solar cells. Progress in Photovoltaics: Research and Applications, 2003, 11(4): 225–230
65. Guillemoles J F. The puzzle of Cu(In, Ga)Se_2 (CIGS) solar cells stability. Thin Solid Films, 2002, 403−404: 405−409
66. Dhere N G. Present status and future prospects of CIGSS thin film solar cells. Solar Energy Materials and Solar Cells, 2006, 90(15): 2181–2190
67. Rau U, Schock H W. Electronic properties of Cu(In, Ga)Se_2 heterojunction solar cells–recent achievements, current understanding, and future challenges. Applied Physics. A, Materials Science & Processing, 1999, 69(2): 131–147
68. Hanna G, Jasenek A, Rau U, et al. Influence of the Ga-content on the bulk defect densities of Cu(In, Ga)Se_2. Thin Solid Films, 2001, 387(1−2): 71–73
69. Singh U P, Patra S P. Progress in polycrystalline thin-film Cu(In, Ga). International Journal of Photoenergy, 2010, 2010: 468147
70. Hiroi H, Iwata Y, Adachi S, et al. New world-record efficiency for pure-sulfide Cu(In, Ga)S_2 thin-film solar cell with Cd-free buffer layer via KCN-free process. IEEE International Journal of Photovoltaics, 2016, 6(3): 760–763
71. Nakamura M, Kouji Y, Chiba Y, et al. Achievement of 19.7% efficiency with a small-sized $Cu(InGa)(SeS)_2$ solar cells prepared by sulfurization after selenizaion process with Zn-based buffer. In: 2013 IEEE 39th Photovoltaic Specialists Conference. Tampa, FL, USA, 2013
72. Kobayashi T, Yamaguchi H, Nakada T. Effects of combined heat and light soaking on device performance of Cu(In, Ga)Se_2solar cells with ZnS(O, OH) buffer layer. Progress in Photovoltaics: Research and Applications, 2014, 22(1): 115–121
73. Kamada R, Yagioka T, Adachi S, et al. New world record Cu(In,

Ga)(Se, S)$_2$ thin film solar cell efficiency beyond 22%. In: 2016 IEEE 43rd Photovoltaic Specialists Conference, Portland, OR, USA, 2016

74. Nakamura M, Yamaguchi K, Kimoto Y, et al. Cd-free Cu(In, Ga)(Se, S)$_2$ thin-film solar cell with record efficiency of 23.35%. IEEE International Journal of Photovoltaics, 2019, 9(6): 1863–1867
75. Yin W, Yang J, Kang J, et al. Halide perovskite materials for solar cells: a theoretical review. Journal of Materials Chemistry. A, Materials for Energy and Sustainability, 2015, 3(17): 8926–8942
76. Ramanujam J, Singh U P. Copper indium gallium selenide based solar cells—a review. Energy & Environmental Science, 2017, 10(6): 1306–1319
77. Li G, Shrotriya V, Huang J, et al. High-efficiency solution processable polymer photovoltaic cells by self-organization of polymer blends. Nature Materials, 2005, 4(11): 864–868
78. Liang Y, Wu Y, Feng D, et al. Development of new semiconducting polymers for high performance solar cells. Journal of the American Chemical Society, 2009, 131(1): 56–57
79. Huo L, Zhang S, Guo X, et al. Replacing alkoxy groups with alkylthienyl groups: a feasible approach to improve the properties of photovoltaic polymers. Angewandte Chemie International Edition, 2011, 50(41): 9697–9702
80. Liao S H, Jhuo H J, Yeh P N, et al. Single junction inverted polymer solar cell reaching power conversion efficiency 10.31% by employing dual-doped zinc oxide nano-film as cathode interlayer. Scientific Reports, 2015, 4(1): 6813
81. Zhao J, Li Y, Yang G, et al. Efficient organic solar cells processed from hydrocarbon solvents. Nature Energy, 2016, 1(2): 15027
82. Bin H, Gao L, Zhang Z, et al. 11.4% Efficiency non-fullerene polymer solar cells with trialkylsilyl substituted 2D-conjugated polymer as donor. Nature Communications, 2016, 7(1): 13651
83. Fei Z, Eisner F D, Jiao X, et al. An alkylated indacenodithieno[3, 2-b]thiophene-based nonfullerene acceptor with high crystallinity exhibiting single junction solar cell efficiencies greater than 13% with low voltage losses. Advanced Materials, 2018, 30(8): 1705209
84. Zhang S, Qin Y, Zhu J, et al. Over 14% efficiency in polymer solar cells enabled by a chlorinated polymer donor. Advanced Materials, 2018, 30(20): 1800868
85. Cui Y, Yao H, Yang C, et al. Organic solar cells with an efficiency approaching 15%. Acta Polymerica Sinica, 2018, 1(2): 223–230 (in Chinese)
86. Meng L, Zhang Y, Wan X, et al. Organic and solution-processed tandem solar cells with 17.3% efficiency. Science, 2018, 361(6407): 1094–1098
87. Xue R, Zhang J, Li Y, et al. Organic solar cell materials toward commercialization. Small, 2018, 14(41): 1801793
88. di Carlo Rasi D, Janssen R A J. Advances in solution-processed multijunction organic solar cells. Advanced Materials, 2019, 31(10): 1806499
89. Zhang C, Wang G, Han H, et al. Self-assembled thin-layer glycomaterials with a proper shell thickness for targeted and activatable cell imaging. Frontiers in Chemistry, 2019, 7: 294
90. Chen W, Zhang Q. Recent progress in non-fullerene small molecule acceptors in organic solar cells (OSCs). Journal of Materials Chemistry. C, Materials for Optical and Electronic Devices, 2017, 5(6): 1275–1302
91. Chen W, Yang X, Long G, et al. A perylene diimide (PDI)-based small molecule with tetrahedral configuration as a non-fullerene acceptor for organic solar cells. Journal of Materials Chemistry. C, Materials for Optical and Electronic Devices, 2015, 3(18): 4698–4705
92. Sun H, Song X, Xie J, et al. PDI derivative through fine-tuning the molecular structure for fullerene-free organic solar cells. ACS Applied Materials & Interfaces, 2017, 9(35): 29924–29931
93. Li C, Zhou J, Song J, et al. Non-fullerene acceptors with branched side chains and improved molecular packing to exceed 18% efficiency in organic solar cells. Nature Energy, 2021, 6(6): 605–613
94. O'Regan B, Grätzel M. A low-cost, high-efficiency solar cell based on dye-sensitized colloidal TiO_2 films. Nature, 1991, 353(6346): 737–740
95. Yeoh M E, Chan K Y. Recent advances in photo-anode for dye-sensitized solar cells: a review. International Journal of Energy Research, 2017, 41(15): 2446–2467
96. Mehmood U, Rahman S U, Harrabi K, et al. Recent advances in dye sensitized solar cells. Advances in Materials Science and Engineering, 2014, 2014: 974782
97. Carella A, Borbone F, Centore R. Research progress on photosensitizers for DSSC. Frontiers in Chemistry, 2018, 6: 481
98. Richhariya G, Kumar A, Tekasakul P, et al. Natural dyes for dye sensitized solar cell: a review. Renewable & Sustainable Energy Reviews, 2017, 69: 705–718
99. Wu J, Lan Z, Lin J, et al. Electrolytes in dye-sensitized solar cells. Chemical Reviews, 2015, 115(5): 2136–2173
100. Iftikhar H, Sonai G G, Hashmi S G, et al. Progress on electrolytes development in dye-sensitized solar cells. Materials (Basel), 2019, 12(12): 1998
101. Zhao Y L, Yao D S, Song C B, et al. CNT–G–TiO_2 layer as a bridge linking TiO_2 nanotube arrays and substrates for efficient dye-sensitized solar cells. RSC Advances, 2015, 5(54): 43805–43809
102. Qiu Y, Chen W, Yang S. Double-layered photoanodes from variable-size anatase TiO_2 nanospindles: a candidate for high-efficiency dye-sensitized solar cells. Angewandte Chemie International Edition, 2010, 49(21): 3675–3679
103. Maheswari D, Venkatachalam P. Fabrication of high efficiency dye-sensitised solar cell with zirconia-doped TiO_2 nanoparticle and nanowire composite photoanode film. Australian Journal of Chemistry, 2015, 68(6): 881
104. Huang Y, Wu H, Yu Q, et al. Single-layer TiO_2 film composed of mesoporous spheres for high-efficiency and stable dye-sensitized solar cells. ACS Sustainable Chemistry & Engineering, 2018, 6(3): 3411–3418
105. Yella A, Lee H W, Tsao H N, et al. Porphyrin-sensitized solar cells with cobalt (II/III)-based redox electrolyte exceed 12 percent efficiency. Science, 2011, 334(6056): 629–634
106. Kyaw A K K, Tantang H, Wu T, et al. Dye-sensitized solar cell with a pair of carbon-based electrodes. Journal of Physics. D,

Applied Physics, 2012, 45(16): 165103
107. Kyaw A K K, Tantang H, Wu T, et al. Dye-sensitized solar cell with a titanium-oxide-modified carbon nanotube transparent electrode. Applied Physics Letters, 2011, 99(2): 021107
108. Tantang H, Kyaw A K K, Zhao Y, et al. Nitrogen-doped carbon nanotube-based bilayer thin film as transparent counter electrode for dye-sensitized solar cells (DSSCs). Chemistry, an Asian Journal, 2012, 7(3): 541–545
109. Liu X, Yang Z, Chueh C C, et al. Improved efficiency and stability of Pb–Sn binary perovskite solar cells by Cs substitution. Journal of Materials Chemistry. A, Materials for Energy and Sustainability, 2016, 4(46): 17939–17945
110. Saliba M, Matsui T, Domanski K, et al. Incorporation of rubidium cations into perovskite solar cells improves photovoltaic performance. Science, 2016, 354(6309): 206–209
111. Kojima A, Teshima K, Shirai Y, et al. Organometal halide perovskites as visible-light sensitizers for photovoltaic cells. Journal of the American Chemical Society, 2009, 131(17): 6050–6051
112. Jeong M, Choi I W, Go E M, et al. Stable perovskite solar cells with efficiency exceeding 24.8% and 0.3-V voltage loss. Science, 2020, 369(6511): 1615–1620
113. Heo J H, Han H J, Kim D, et al. Hysteresis-less inverted $CH_3NH_3PbI_3$ planar perovskite hybrid solar cells with 18.1% power conversion efficiency. Energy & Environmental Science, 2015, 8(5): 1602–1608
114. Mali S S, Kim H, Kim H H, et al. Nanoporous p-type NiO_x electrode for p-i-n inverted perovskite solar cell toward air stability. Materials Today, 2018, 21(5): 483–500
115. Chan S H, Wu M C, Lee K, et al. Enhancing perovskite solar cell performance and stability by doping Barium in methylammonium lead halide. Journal of Materials Chemistry. A, Materials for Energy and Sustainability, 2017, 5(34): 18044–18052
116. Wu M C, Chan S H, Lee K, et al. Enhancing the efficiency of perovskite solar cells using mesoscopic zinc-doped TiO_2 as the electron extraction layer through band alignment. Journal of Materials Chemistry. A, Materials for Energy and Sustainability, 2018, 6(35): 16920–16931
117. Chan S H, Chang Y H, Wu M C. High-performance perovskite solar cells based on low-temperature processed electron extraction layer. Frontiers in Materials, 2019, 6: 57
118. Dubey A, Adhikari N, Mabrouk S, et al. A strategic review on processing routes towards highly efficient perovskite solar cells. Journal of Materials Chemistry. A, Materials for Energy and Sustainability, 2018, 6(6): 2406–2431
119. Noh J H, Im S H, Heo J H, et al. Chemical management for colorful, efficient, and stable inorganic-organic hybrid nanostructured solar cells. Nano Letters, 2013, 13(4): 1764–1769
120. Im J H, Lee C R, Lee J W, et al. 6.5% efficient perovskite quantum-dot-sensitized solar cell. Nanoscale, 2011, 3(10): 4088
121. Kim H S, Lee C R, Im J H, et al. Lead iodide perovskite sensitized all-solid-state submicron thin film mesoscopic solar cell with efficiency exceeding 9%. Scientific Reports, 2012, 2(1): 591
122. Lee M M, Teuscher J, Miyasaka T, et al. Efficient hybrid solar cells based on meso-superstructured organometal halide perovskites. Science, 2012, 338(6107): 643–647
123. Wang J T W, Ball J M, Barea E M, et al. Low-temperature processed electron collection layers of graphene/TiO_2 nanocomposites in thin film perovskite solar cells. Nano Letters, 2014, 14(2): 724–730
124. Liu D, Kelly T L. Perovskite solar cells with a planar heterojunction structure prepared using room-temperature solution processing techniques. Nature Photonics, 2014, 8(2): 133–138
125. Klug M T, Osherov A, Haghighirad A A, et al. Tailoring metal halide perovskites through metal substitution: influence on photovoltaic and material properties. Energy & Environmental Science, 2017, 10(1): 236–246
126. Abdelhady A L, Saidaminov M I, Murali B, et al. Heterovalent dopant incorporation for bandgap and type engineering of perovskite crystals. Journal of Physical Chemistry Letters, 2016, 7(2): 295–301
127. Wang Z, Li M, Yang Y, et al. High efficiency Pb-in binary metal perovskite solar cells. Advanced Materials, 2016, 28(31): 6695–6703
128. Chang J, Lin Z, Zhu H, et al. Enhancing the photovoltaic performance of planar heterojunction perovskite solar cells by doping the perovskite layer with alkali metal ions. Journal of Materials Chemistry. A, Materials for Energy and Sustainability, 2016, 4(42): 16546–16552
129. Wang J T W, Wang Z, Pathak S, et al. Efficient perovskite solar cells by metal ion doping. Energy & Environmental Science, 2016, 9(9): 2892–2901
130. van der Stam W, Geuchies J J, Altantzis T, et al. Highly emissive divalent-ion-doped colloidal $CsPb_{1-x}M_xBr_3$ perovskite nanocrystals through cation exchange. Journal of the American Chemical Society, 2017, 139(11): 4087–4097
131. Kour R, Arya S, Verma S, et al. Potential substitutes for replacement of lead in perovskite solar cells: a review. Global Challenges (Hoboken, NJ), 2019, 3(11): 1900050
132. Hao F, Stoumpos C C, Chang R P H, et al. Anomalous band gap behavior in mixed Sn and Pb perovskites enables broadening of absorption spectrum in solar cells. Journal of the American Chemical Society, 2014, 136(22): 8094–8099
133. Zuo F, Williams S T, Liang P, et al. Binary-metal perovskites toward high-performance planar-heterojunction hybrid solar cells. Advanced Materials, 2014, 26(37): 6454–6460
134. Stoumpos C C, Malliakas C D, Kanatzidis M G. Semiconducting tin and lead iodide perovskites with organic cations: phase transitions, high mobilities, and near-infrared photoluminescent properties. Inorganic Chemistry, 2013, 52(15): 9019–9038
135. Babayigit A, Duy Thanh D, Ethirajan A, et al. Assessing the toxicity of Pb- and Sn-based perovskite solar cells in model organism Danio rerio. Scientific Reports, 2016, 6(1): 18721
136. Kooijman M, Muscarella L A, Williams R M. Perovskite thin film materials stabilized and enhanced by zinc(II) doping. Applied Sciences (Basel, Switzerland), 2019, 9(8): 1678
137. Chen R, Hou D, Lu C, et al. Zinc ion as effective film

morphology controller in perovskite solar cells. Sustainable Energy & Fuels, 2018, 2(5): 1093–1100
138. Zheng H, Liu G, Xu X, et al. Acquiring high-performance and stable mixed-dimensional perovskite solar cells by using a transition-metal-substituted Pb precursor. ChemSusChem, 2018, 11(18): 3269–3275
139. Shai X, Wang J, Sun P, et al. Achieving ordered and stable binary metal perovskite via strain engineering. Nano Energy, 2018, 48: 117–127
140. Jung E H, Jeon N J, Park E Y, et al. Efficient, stable and scalable perovskite solar cells using poly(3-hexylthiophene). Nature, 2019, 567(7749): 511–515
141. Said A A, Xie J, Zhang Q. Recent progress in organic electron transport materials in inverted perovskite solar cells. Small, 2019, 15(27): 1900854
142. Gu P, Wang N, Wu A, et al. An azaacene derivative as promising electron-transport layer for inverted perovskite solar cells. Chemistry, an Asian Journal, 2016, 11(15): 2135–2138
143. Gu P, Wang N, Wang C, et al. Pushing up the efficiency of planar perovskite solar cells to 18.2% with organic small molecules as the electron transport layer. Journal of Materials Chemistry. A, Materials for Energy and Sustainability, 2017, 5(16): 7339–7344
144. Jeong J, Kim M, Seo J, et al. Pseudo-halide anion engineering for α-$FAPbI_3$ perovskite solar cells. Nature, 2021, 592(7854): 381–385
145. Tsakalakos L. Nanotechnology for Photovoltaics. New York: CRC Press, 2010
146. Guha S. Thin film silicon solar cells grown near the edge of amorphous to microcrystalline transition. Solar Energy, 2004, 77(6): 887–892
147. Yamaguchi M, Nishimura K I, Sasaki T, et al. Novel materials for high-efficiency III–V multi-junction solar cells. Solar Energy, 2008, 82(2): 173–180
148. Takamoto T, Washio H, Juso H. Application of InGaP/GaAs/InGaAs triple junction solar cells to space use and concentrator photovoltaic. In: 2014 IEEE 40th Photovoltaic Specialist Conference, Denver, CO, USA, 2014
149. Dimroth F, Tibbits T N D, Niemeyer M, et al. Four-junction wafer-bonded concentrator solar cells. IEEE International Journal of Photovoltaics, 2016, 6(1): 343–349
150. Geisz J F, Steiner M A, Jain N, et al. Building a six-junction inverted metamorphic concentrator solar cell. IEEE International Journal of Photovoltaics, 2018, 8(2): 626–632
151. Gul M, Kotak Y, Muneer T. Review on recent trend of solar photovoltaic technology. Energy Exploration & Exploitation, 2016, 34(4): 485–526
152. Muteri V, Cellura M, Curto D, et al. Review on life cycle assessment of solar photovoltaic panels. Energies, 2020, 13(1): 252
153. Andreani L C, Bozzola A, Kowalczewski P, et al. Silicon solar cells: toward the efficiency limits. Advances in Physics: X, 2019, 4(1): 1548305
154. Yang D, Zhang X, Hou Y, et al. 28.3%-efficiency perovskite/silicon tandem solar cell by optimal transparent electrode for high efficient semitransparent top cell. Nano Energy, 2021, 84: 105934
155. Al-Ashouri A, Köhnen E, Li B, et al. Monolithic perovskite/silicon tandem solar cell with >29% efficiency by enhanced hole extraction. Science, 2020, 370(6522): 1300–1309
156. Xu J, Boyd C C, Yu Z J, et al. Triple-halide wide-band gap perovskites with suppressed phase segregation for efficient tandems. Science, 2020, 367(6482): 1097–1104
157. Hou Y, Aydin E, de Bastiani M, et al. Efficient tandem solar cells with solution-processed perovskite on textured crystalline silicon. Science, 2020, 367(6482): 1135–1140
158. Chen B, Yu Z J, Manzoor S, et al. Blade-coated perovskites on textured silicon for 26%-efficient monolithic perovskite/silicon tandem solar cells. Joule, 2020, 4(4): 850–864
159. Wang Z, Zhu X, Zuo S, et al. 27%-efficiency four-terminal perovskite/silicon tandem solar cells by sandwiched gold nanomesh. Advanced Functional Materials, 2020, 30(4): 1908298
160. Werner S, Lohmüller E, Maier S, et al. Challenges for lowly-doped phosphorus emitters in silicon solar cells with screen-printed silver contacts. Energy Procedia, 2017, 124: 936–946
161. Vak D, Kim S S, Jo J, et al. Fabrication of organic bulk heterojunction solar cells by a spray deposition method for low-cost power generation. Applied Physics Letters, 2007, 91(8): 081102
162. Hoth C N, Steim R, Schilinsky P, et al. Topographical and morphological aspects of spray coated organic photovoltaics. Organic Electronics, 2009, 10(4): 587–593
163. Girotto C, Moia D, Rand B P, et al. High-performance organic solar cells with spray-coated hole-transport and active layers. Advanced Functional Materials, 2011, 21(1): 64–72
164. Kang J W, Kang Y, Jung S, et al. Fully spray-coated inverted organic solar cells. Solar Energy Materials and Solar Cells, 2012, 103: 76–79
165. Wang T, Scarratt N W, Yi H, et al. Fabricating high performance, donor-acceptor copolymer solar cells by spray-coating in air. Advanced Energy Materials, 2013, 3(4): 505–512
166. Zhang Y, Griffin J, Scarratt N W, et al. High efficiency arrays of polymer solar cells fabricated by spray-coating in air. Progress in Photovoltaics: Research and Applications, 2016, 24(3): 275–282
167. Barrows A T, Pearson A J, Kwak C K, et al. Efficient planar heterojunction mixed-halide perovskite solar cells deposited via spray-deposition. Energy & Environmental Science, 2014, 7(9): 2944–2950
168. Das S, Yang B, Gu G, et al. High-performance flexible perovskite solar cells by using a combination of ultrasonic spray-coating and low thermal budget photonic curing. ACS Photonics, 2015, 2(6): 680–686
169. Tait J G, Manghooli S, Qiu W, et al. Rapid composition screening for perovskite photovoltaics via concurrently pumped ultrasonic spray coating. Journal of Materials Chemistry. A, Materials for Energy and Sustainability, 2016, 4(10): 3792–3797
170. Huang H, Shi J, Zhu L, et al. Two-step ultrasonic spray deposition of $CH_3NH_3PbI_3$ for efficient and large-area perovskite solar cell. Nano Energy, 2016, 27: 352–358
171. Heo J H, Lee M H, Jang M H, et al. Highly efficient

$CH_3NH_3PbI_{3-x}Cl_x$ mixed halide perovskite solar cells prepared by re-dissolution and crystal grain growth via spray coating. Journal of Materials Chemistry. A, Materials for Energy and Sustainability, 2016, 4(45): 17636–17642

172. Mohamad D K, Griffin J, Bracher C, et al. Spray-cast multilayer organometal perovskite solar cells fabricated in air. Advanced Energy Materials, 2016, 6(22): 1600994
173. Bishop J E, Mohamad D K, Wong-Stringer M, et al. Spray-cast multilayer perovskite solar cells with an active-area of 1.5 cm^2. Scientific Reports, 2017, 7(1): 7962
174. Hu Z, Zhang J, Xiong S, et al. Performance of polymer solar cells fabricated by dip coating process. Solar Energy Materials and Solar Cells, 2012, 99: 221–225
175. Hu Z, Zhang J, Xiong S, et al. Annealing-free, air-processed and high-efficiency polymer solar cells fabricated by a dip coating process. Organic Electronics, 2012, 13(1): 142–146
176. Harun W S W, Asri R I M, Alias J, et al. A comprehensive review of hydroxyapatite-based coatings adhesion on metallic biomaterials. Ceramics International, 2018, 44(2): 1250–1268
177. Aziz F, Ismail A F. Spray coating methods for polymer solar cells fabrication: a review. Materials Science in Semiconductor Processing, 2015, 39: 416–425
178. Li L, Gao P, Schuermann K C, et al. Controllable growth and field-effect property of monolayer to multilayer microstripes of an organic semiconductor. Journal of the American Chemical Society, 2010, 132(26): 8807–8809
179. Roland S, Pellerin C, Bazuin C G, et al. Evolution of small molecule content and morphology with dip-coating rate in supramolecular PS–P4VP thin films. Macromolecules, 2012, 45(19): 7964–7972
180. Chou C S, Chou F, Kang J Y. Preparation of ZnO-coated TiO_2 electrodes using dip coating and their applications in dye-sensitized solar cells. Powder Technology, 2012, 215−216: 38−45
181. Adnan M, Lee J K. All sequential dip-coating processed perovskite layers from an aqueous lead precursor for high efficiency perovskite solar cells. Scientific Reports, 2018, 8(1): 2168
182. Adnan M, Lee J K. Highly efficient planar heterojunction perovskite solar cells with sequentially dip-coated deposited perovskite layers from a non-halide aqueous lead precursor. RSC Advances, 2020, 10(9): 5454–5461
183. Adnan M, Irshad Z, Lee J K. Facile all-dip-coating deposition of highly efficient $(CH_3)_3NPbI_{3-x}Cl_x$ perovskite materials from aqueous non-halide lead precursor. RSC Advances, 2020, 10(48): 29010–29017
184. Gao T, Jelle B P. Nanoelectrochromics for smart windows: materials and methodologies. In: Proceedings of the TechConnect World Innovation Conference 2016, Washington DC: USA, 2016
185. Razza S, Castro-Hermosa S, di Carlo A, et al. Research update: large-area deposition, coating, printing, and processing techniques for the upscaling of perovskite solar cell technology. APL Materials, 2016, 4(9): 091508
186. Williams S T, Rajagopal A, Chueh C C, et al. Current challenges and prospective research for upscaling hybrid perovskite photovoltaics. Journal of Physical Chemistry Letters, 2016, 7(5): 811–819
187. Chen W, Wu Y, Yue Y, et al. Efficient and stable large-area perovskite solar cells with inorganic charge extraction layers. Science, 2015, 350(6263): 944–948
188. Cui Y, Yao H, Hong L, et al. Organic photovoltaic cell with 17% efficiency and superior processability. National Science Review, 2020, 7(7): 1239–1246
189. Yang M, Zhou Y, Zeng Y, et al. Square-centimeter solution-processed planar $CH_3NH_3PbI_3$ perovskite solar cells with efficiency exceeding 15%. Advanced Materials, 2015, 27(41): 6363–6370
190. Qiu W, Merckx T, Jaysankar M, et al. Pinhole-free perovskite films for efficient solar modules. Energy & Environmental Science, 2016, 9(2): 484–489
191. Agresti A, Pescetelli S, Palma A L, et al. Graphene interface engineering for perovskite solar modules: 12.6% power conversion efficiency over 50 cm^2 active area. ACS Energy Letters, 2017, 2(1): 279–287
192. Swartwout R, Hoerantner M T, Bulović V. Scalable deposition methods for large-area production of perovskite thin films. Energy & Environmental Materials, 2019, 2(2): 119–145
193. Ding X, Liu J, Harris T A L. A review of the operating limits in slot die coating processes. AIChE Journal, 2016, 62(7): 2508–2524
194. Carvalho M S, Kheshgi H S. Low-flow limit in slot coating: theory and experiments. AIChE Journal, 2000, 46(10): 1907–1917
195. Patidar R, Burkitt D, Hooper K, et al. Slot-die coating of perovskite solar cells: an overview. Materials Today Communications, 2020, 22: 100808
196. Hwang K, Jung Y S, Heo Y J, et al. Toward large scale roll-to-roll production of fully printed perovskite solar cells. Advanced Materials, 2015, 27(7): 1241–1247
197. di Giacomo F, Shanmugam S, Fledderus H, et al. Up-scalable sheet-to-sheet production of high efficiency perovskite module and solar cells on 6-in. substrate using slot die coating. Solar Energy Materials and Solar Cells, 2018, 181: 53–59
198. Burkitt D, Searle J, Watson T. Perovskite solar cells in NIP structure with four slot-die-coated layers. Royal Society Open Science, 2018, 5(5): 172158
199. Lee D, Jung Y S, Heo Y J, et al. Slot-die coated perovskite films using mixed lead precursors for highly reproducible and large-area solar cells. ACS Applied Materials & Interfaces, 2018, 10(18): 16133–16139
200. Heo Y J, Kim J E, Weerasinghe H, et al. Printing-friendly sequential deposition via intra-additive approach for roll-to-roll process of perovskite solar cells. Nano Energy, 2017, 41: 443–451
201. Kim Y Y, Park E Y, Yang T Y, et al. Fast two-step deposition of perovskite via mediator extraction treatment for large-area, high-performance perovskite solar cells. Journal of Materials Chemistry. A, Materials for Energy and Sustainability, 2018, 6(26): 12447–12454
202. Dou B, Whitaker J B, Bruening K, et al. Roll-to-roll printing of perovskite solar cells. ACS Energy Letters, 2018, 3(10):

2558–2565

203. Yang Z, Chueh C C, Zuo F, et al. High-performance fully printable perovskite solar cells via blade-coating technique under the ambient condition. Advanced Energy Materials, 2015, 5(13): 1500328
204. Qiao F, Xie Y, He G, et al. Light trapping structures and plasmons synergistically enhance the photovoltaic performance of full-spectrum solar cells. Nanoscale, 2020, 12(3): 1269–1280
205. Zhao J, Green M A. Optimized antireflection coatings for high-efficiency silicon solar cells. IEEE Transactions on Electron Devices, 1991, 38(8): 1925–1934
206. Xi J Q, Schubert M F, Kim J K, et al. Optical thin-film materials with low refractive index for broadband elimination of Fresnel reflection. Nature Photonics, 2007, 1(3): 176–179
207. Koynov S, Brandt M S, Stutzmann M. Black nonreflecting silicon surfaces for solar cells. Applied Physics Letters, 2006, 88(20): 203107
208. Huang Y, Chattopadhyay S, Jen Y J, et al. Improved broadband and quasi-omnidirectional anti-reflection properties with biomimetic silicon nanostructures. Nature Nanotechnology, 2007, 2(12): 770–774
209. Zhu J, Yu Z, Burkhard G F, et al. Optical absorption enhancement in amorphous silicon nanowire and nanocone arrays. Nano Letters, 2009, 9(1): 279–282
210. Jeong S, Garnett E C, Wang S, et al. Hybrid silicon nanocone-polymer solar cells. Nano Letters, 2012, 12(6): 2971–2976
211. Tsakalakos L, Balch J, Fronheiser J, et al. Silicon nanowire solar cells. Applied Physics Letters, 2007, 91(23): 233117
212. Fan Z, Kapadia R, Leu P W, et al. Ordered arrays of dual-diameter nanopillars for maximized optical absorption. Nano Letters, 2010, 10(10): 3823–3827
213. Berger O, Inns D, Aberle A G. Commercial white paint as back surface reflector for thin-film solar cells. Solar Energy Materials and Solar Cells, 2007, 91(13): 1215–1221
214. Ye L, Zhang Y, Zhang X, et al. Sol-gel preparation of $SiO_2/TiO_2/SiO_2$-TiO_2 broadband antireflective coating for solar cell cover glass. Solar Energy Materials and Solar Cells, 2013, 111: 160–164
215. Chen J, Wang S, Sun Q, et al. Light-manipulation schemes: a facile solution-processed light manipulation structure for organic solar cells. Advanced Optical Materials, 2019, 7(2): 1970006
216. Liyanage W P R, Nath M. CdS–CdTe heterojunction nanotube arrays for efficient solar energy conversion. Journal of Materials Chemistry. A, Materials for Energy and Sustainability, 2016, 4(38): 14637–14648
217. Zhuang T, Liu Y, Li Y, et al. Integration of semiconducting sulfides for full-spectrum solar energy absorption and efficient charge separation. Angewandte Chemie International Edition, 2016, 55(22): 6396–6400
218. Jošt M, Albrecht S, Kegelmann L, et al. Efficient light management by textured nanoimprinted layers for perovskite solar cells. ACS Photonics, 2017, 4(5): 1232–1239
219. Myers J D, Cao W, Cassidy V, et al. A universal optical approach to enhancing efficiency of organic-based photovoltaic devices. Energy & Environmental Science, 2012, 5(5): 6900
220. Chen J, Jin T, Li Y, et al. Recent progress of light manipulation strategies in organic and perovskite solar cells. Nanoscale, 2019, 11(40): 18517–18536
221. Day J, Senthilarasu S, Mallick T K. Improving spectral modification for applications in solar cells: a review. Renewable Energy, 2019, 132: 186–205
222. Ali N M, Rafat N H. Modeling and simulation of nanorods photovoltaic solar cells: a review. Renewable & Sustainable Energy Reviews, 2017, 68: 212–220
223. Atwater H A, Polman A. Plasmonics for improved photovoltaic devices. Nature Materials, 2010, 9(3): 205–213
224. Mandal P, Sharma S. Progress in plasmonic solar cell efficiency improvement: a status review. Renewable & Sustainable Energy Reviews, 2016, 65: 537–552
225. Pala R A, White J, Barnard E, et al. Design of plasmonic thin-film solar cells with broadband absorption enhancements. Advanced Materials, 2009, 21(34): 3504–3509
226. Lee Y C, Huang C F, Chang J Y, et al. Enhanced light trapping based on guided mode resonance effect for thin-film silicon solar cells with two filling-factor gratings. Optics Express, 2008, 16(11): 7969–7975
227. Chao C C, Wang C M, Chang Y C, et al. Plasmonic multilayer structure for ultrathin amorphous silicon film photovoltaic cell. Optical Review, 2009, 16(3): 343–346
228. Rockstuhl C, Fahr S, Lederer F. Absorption enhancement in solar cells by localized plasmon polaritons. Journal of Applied Physics, 2008, 104(12): 123102
229. Bai W, Gan Q, Bartoli F, et al. Design of plasmonic back structures for efficiency enhancement of thin-film amorphous Si solar cells. Optics Letters, 2009, 34(23): 3725
230. Ferry V E, Verschuuren M A, Li H B T, et al. Improved red-response in thin film a-Si: H solar cells with soft-imprinted plasmonic back reflectors. Applied Physics Letters, 2009, 95(18): 183503
231. Sai H, Fujiwara H, Kondo M. Back surface reflectors with periodic textures fabricated by self-ordering process for light trapping in thin-film microcrystalline silicon solar cells. Solar Energy Materials and Solar Cells, 2009, 93(6−7): 1087–1090
232. Mokkapati S, Beck F J, Polman A, et al. Designing periodic arrays of metal nanoparticles for light-trapping applications in solar cells. Applied Physics Letters, 2009, 95(5): 053115
233. Mendes M J, Morawiec S, Simone F, et al. Colloidal plasmonic back reflectors for light trapping in solar cells. Nanoscale, 2014, 6(9): 4796–4805
234. Nakayama K, Tanabe K, Atwater H A. Plasmonic nanoparticle enhanced light absorption in GaAs solar cells. Applied Physics Letters, 2008, 93(12): 121904
235. Skrabalak S E, Chen J, Sun Y, et al. Gold nanocages: synthesis, properties, and applications. Accounts of Chemical Research, 2008, 41(12): 1587–1595
236. Lee D S, Kim W, Cha B G, et al. Self-position of Au NPs in perovskite solar cells: optical and electrical contribution. ACS Applied Materials & Interfaces, 2016, 8(1): 449–454
237. Yuan Z, Wu Z, Bai S, et al. Perovskite solar cells: hot-electron injection in a sandwiched TiO_x-Au-TiO_x structure for high-performance planar perovskite solar cells. Advanced Energy Materials, 2015, 5(10): 1500038

238. Reineck P, Brick D, Mulvaney P, et al. Plasmonic hot electron solar cells: the effect of nanoparticle size on quantum efficiency. Journal of Physical Chemistry Letters, 2016, 7(20): 4137–4141
239. Schaadt D M, Feng B, Yu E T. Enhanced semiconductor optical absorption via surface plasmon excitation in metal nanoparticles. Applied Physics Letters, 2005, 86(6): 063106
240. Xu Z, Lin Y, Yin M, et al. Nanotubes: understanding the enhancement mechanisms of surface plasmon-mediated photoelectrochemical electrodes: a case study on Au nanoparticle decorated TiO_2 nanotubes. Advanced Materials Interfaces, 2015, 2(13): 1500169
241. Chen S, Wang Y, Liu Q, et al. Broadband enhancement of PbS quantum dot solar cells by the synergistic effect of plasmonic gold nanobipyramids and nanospheres. Advanced Energy Materials, 2018, 8(8): 1701194
242. Srivastava A, Samajdar D P, Sharma D. Plasmonic effect of different nanoarchitectures in the efficiency enhancement of polymer based solar cells: a review. Solar Energy, 2018, 173: 905–919
243. Edinbarough I. Experimental study on the optimum harvesting of sunlight for an efficient solar energy system. In: 2013 ASEE Annual Conference & Exposition Proceedings, Atlanta, Georgia, USA, 2013
244. Kvasznicza Z, Elmer G. Optimizing solar tracking systems for solar cells. In: Proceeding of 4th Serbian–Hungarian joint Symposium on Intelligent Systems, 2006
245. Mousazadeh H, Keyhani A, Javadi A, et al. A review of principle and sun-tracking methods for maximizing solar systems output. Renewable & Sustainable Energy Reviews, 2009, 13(8): 1800–1818
246. Luque-Heredia I, Moreno J, Magalhaes P, et al. Inspira's CPV sun tracking. In: Luque, A L, Andreev V M, eds. Concentrator Photovoltaics. Berlin, Heidelberg: Springer, 2007
247. García-Segura A, Fernández-García A, Ariza M J, et al. Durability studies of solar reflectors: a review. Renewable & Sustainable Energy Reviews, 2016, 62: 453–467
248. Wiesinger F, Sutter F, Fernández-García A, et al. Sand erosion on solar reflectors: accelerated simulation and comparison with field data. Solar Energy Materials and Solar Cells, 2016, 145: 303–313
249. Kennedy C E, Terwilliger K. Optical durability of candidate solar reflectors. Journal of Solar Energy Engineering, 2005, 127(2): 262–269
250. Kennedy C E, Terwilliger K, Jorgensen G J. Analysis of accelerated exposure testing of thin-glass mirror matrix. In: Proceedings of ASME 2005 International Solar Energy Conference, Orlando, Florida, USA, 2008
251. Almanza R, Hernández P, Martínez I, et al. Development and mean life of aluminum first-surface mirrors for solar energy applications. Solar Energy Materials and Solar Cells, 2009, 93(9): 1647–1651
252. Price H, Lu¨pfert E, Kearney D, et al. Advances in parabolic trough solar power technology. Journal of Solar Energy Engineering, 2002, 124(2): 109–125
253. Xie W T, Dai Y J, Wang R Z, et al. Concentrated solar energy applications using Fresnel lenses: a review. Renewable & Sustainable Energy Reviews, 2011, 15(6): 2588–2606
254. Kumar V, Shrivastava R L, Untawale S P. Fresnel lens: a promising alternative of reflectors in concentrated solar power. Renewable & Sustainable Energy Reviews, 2015, 44: 376–390
255. Miller D C, Kurtz S R. Durability of Fresnel lenses: a review specific to the concentrating photovoltaic application. Solar Energy Materials and Solar Cells, 2011, 95(8): 2037–2068